COMPUTATIONAL ANALYSIS OF VARIOUS THERMAL BARRIER COATINGS ON STEEL SURFACE

A project report submitted to
Jawaharlal Nehru Technological UniversityHyderabad
in partial fulfillment of the requirements for the award of the degree of

BACHELOR OF TECHNOLOGY

In

MECHANICAL ENGINEERING

Submitted By

P.SIVA MALLIKARJUN :18WJ1A03F3

P.NARASIMHA RAO NAIDU :18WJ1A03F6

P.HARSHITH REDDY :18WJ1A03F8

Under the Guidance of

Dr. M. RAMALINGA REDDY

Director, GNITC

&

Dr. S. NAGAKALYAN

Professor, Department of Mechanical Engineering

DEPARTMENT OF MECHANICAL ENGINEERING

GURU NANAK INSTITUTIONS TECHNICAL CAMPUS (AUTONOMOUS)

(Affiliated to JNTU, Hyderabad, Approved by AICTE, New Delhi)

Ibrahimpatnam, Ranga Reddy District -501506

Telangana, India.

2021-2022

CERTIFICATE

This is to certify that the Mini-Project entitled "**COMPUTATIONAL ANYASLSIS OF VARIOUS THERMAL BARRIER COATINGSON STEEL SURFACE**" is being submitted by **Mr. P. SIVA MALIKARJUN (18WJ1A03F3), Mr. P. NARASIMHA RAO NAIDU (18WJ1A03F6), Mr. P.HARSHITH REDDY (18WJ1A03F8)** in partial fulfillment for the award of the **Degree of Bachelor of Technology in Mechanical Engineering to the Jawaharlal Nehru Technological University Hyderabad** is a record of bonafide work carried out by them under my guidance and supervision.

The results embodied in this Mini-Project report have not been submitted to any other University or Institute for the award of any Degree or Diploma

Internal Guide
Dr. S. NAGAKALYAN
Professor

External Examiner

Head of the Department
(MECHANICAL ENGINEERING)

DECLARATION

We declare that this Mini-Project report titled "**COMPUTATIONAL ANYASLSIS OF VARIOUS THERMAL BARRIER COATINGS ON STEEL SURFACE"** submitted in partial fulfillment for the award of the **Degree of Bachelor of Technology in Mechanical Engineering to the Jawaharlal Nehru Technological University Hyderabad** is a record of original work carried out us under the guidance of **Dr. S. NAGAKALYAN, Professor, Department of Mechanical Engineering,** and has not formed the basis for the award of any other degree or diploma, in this or any other Institution or University. In keeping with the ethical practice in reporting scientific information, due acknowledgements have been made whenever the findings of others have been cited.

P. SIVA MALLIKARJUN
(18WJ1A03F3)

P. NARASIMHA RAO NAIDU
(18WJ1A03F6)

P.HARSHITH REDDY
(18WJ1A03F8)

ACKNOWLEDGEMENTS

We wish to express our sincere thanks to **Dr. H.S. SAINI,** Managing Director, Guru Nanak Institutions and **Dr. M. RAMALINGA REDDY,** Director, Guru Nanak Institutions Technical Campus, School of Engineering and Technology, for providing us with all the necessary facilities and their support.

We place on record, our sincere thanks to **Dr. A. RAJ KUMAR**, Professors and Head of the Department, Mechanical Engineering for their whole-hearted co-operation, providing excellent lab facility, constant encouragement and unfailing inspiration.

We would like to say sincere thanks to **Dr. S. NAGAKALYAN**, Professor, and Department of Mechanical Engineering for coordinating Projects

We especially thank our internal guide **Dr. S. NAGAKALYAN,** Professor, Department of Mechanical Engineering for the suggestions and constant guidance in every stage of the project. We also like to thank all of our faculties helping us in every possible way.

On a more personal note we thank our **BELOVED PARENTS** and **FRIENDS** for their moral support during the course of our project.

P. SIVA MALLIKARJUN : (18WJ1A03F3)
P.NARASIMHA RAO NAIDU : (18WJ1A03F6)
P.HARSHITH REDDY : (18WJ1A03F8)

ABSTRACT

The Main Objective is to choose the better variant TBC among the other TBC'S which is computed. The better variant TBC will be more in heat dissipation. The TBC are applied for need to tinny surfaces operational at elevated temperatures, as a variety of exhaust heat management. We use Steel AISL4340 as the metal substrate in TBCs coatings. Thermal barrier coatings (TBCs) area unit advanced materials systems typically applied to tinny surfaces operational at elevated temperatures, as a variety of exhaust heat management. The heat barrier coatings resist the thermal conduction by adding composite materials and increasing the heat barrier temperature in numerous fields like a turbine or aero-engine components, area crafts, rocket –jet engines, jet propellers etc.

The heat barrier systems use numerous ceramic constituents to form a barrier to the temperatures tough operational. They are doing not type a barrier to hot corrosion and chemical reaction merchandise however do act as an insulation layer reducing the results of thermal conduction. In these TBC's the materials area unit applied like composites of Amorphous Al_2O_3, Amorphous MoO_3, Amorphous TiO_2, Pure ZrO_2,7-8YSZ and a few

Compositions severally were doped with Yttria-stabilized Zirconia (YSZ) to create a TBC layer on the steel surface. Those were computed severally. According to the Finite component Analysis, the composition of Pure ZrO_2 doped with YSZ TBC have higher performance within the temperature of heat barrier compare to different TBC's severally.

CONTENTS

LIST OF FIGURES

LIST OF TABLES

CHAPTER 1
INTRODUCTION

1.1 Introduction

During the past decade, research reports were devoted to the development and manufacturing of ceramic thermal barrier coatings (TBCs) on turbine parts because the traditional turbine material has reached the limits of their temperature capabilities. TBCs are deposited on transition pieces, combustion lines, first-stage blades, and vanes and other hot- path components of gas turbines either to increase the inlet temperature with a consequent improvement of the efficiency or to reduce the requirements for the cooling system.

The earliest ceramic coatings for aerospace applications were frit enamels developed by the National Advisory Committee for Aeronautics (NACA) and the coating of calcium stabilized zirconia on the exhaust nozzle of the X-15 manned rocket plane in the 1960s is believed to be the first use of TBCs in manned flight. The working parts of aircraft jet engines are subjected to serve mechanical, chemical and thermal stresses. Several ceramic coatings such as Al_2O_3, TiO_2, mullite, CaO/ MgO+ZrO_2, YSZ, CeO_2+YSZ, zircon, and $La_2Zr_2O_7$, etc. have been evaluated as TBC materials.

Definition to thermal barrier Coatings:

Generally, the TBC system consists of a ceramic top coating, a metallic bond coating and a metallic substrate . Usually, M-NiCrY type bond coating is applied to assist the adherence and stress relaxation. However, exposure of the TBC system to elevated temperatures leads to the development of a thermally grown oxide (TGO) layer between the bond coating and top coating . TGO has a major influence on the TBC durability. As the TGO layer thickness increases with the operation time, high stresses are generated at the bond coating/TGO interface due to the volume increase, thermal expansion misfit and applied loads. As a consequence, crack initiates and propagates, leading to the spallation of ceramics.

The ceramic top coating, finally resulting in the failure of the TBC system . Thus, the bond coating is the most critical component of the TBC system. The chemistry and microstructure of bond coating affect the durability through the structure and morphology of the developed TGO

Glass ceramic coatings possess excellent chemical inertness, low thermal conductivity, high-temperature stability and superior mechanical properties. Because of the excellent combination of these properties, glass ceramic coatings can efficiently be utilized to reduce high-temperature degradation of the structural materials.

Further, the glass ceramic coating is also conceived as cheap but effective alternative thermal barrier coating.The selection of TBC materials is restricted by some basic requirements: (1) high melting point, (2) no phase transformation between room temperature and operating temperature, (3) low thermal conductivity, (4) chemical inertness, (5) thermal expansion match with the metallic substrate, (6) good adherence

to the metallic substrate and (7) low sintering rate of the porous microstructure [1-5]. The number of materials that can be used as TBCs is very limited. So far, only a few materials have been found to basically satisfy these requirements.

In recent years metal oxide doped yttria stabilized zirconia glassy phase showed good performance as a thermal barrier coating [8]. The inherent low thermal conductivity of the glass ceramic based bond coating can reduce the metal substrate temperature and thereby protect the substrate from oxidation and creep failure. Therefore, glass ceramics may be an ideal bond coating in a TBC system. Potential of glass ceramics as good oxidation and thermal shock resistant bond coating in the conventional thermal barrier coating system has been already established [9-11].

First-principles quantum mechanics simulations are very useful to develop the TBC materials. With help of computational methods, we can predict how to produce high-temperature coatings that protect turbine engine components vital for electricity production and transportation. Many simulation methods based on quantum mechanics exist; here we primarily used Kohn–Sham density functional theory (DFT) as implemented in the CASTEP and VASP codes. DFT is advantageous because it permits the use of periodic boundary conditions to simulate large crystals while usually providing a good balance between accuracy and computational expense.

CHAPTER 2

LITERATURE SURVEY

Computational Analysis of a thermal barrier coating is coated composites are incorporated in Rietveld HM (1967) Line profiles of neutron powder-diffraction peaks for structure refinement. Acta Crystallogr 22(1):151-152. In this paper the thermal stability, structural and dielectric properties of the (CaTiO3)1-x(Cr3/4Fe5/4O3)x ceramic composites with x = 0, 0.1, 0.5, 0.9 and 1 have been examined in microwave region. The samples were produced via the solid-state reaction.

The orthorhombic structural phase of CaTiO3 and trigonal structural phase of Cr3/4Fe5/4O3 were confirmed by the X-Ray Powder Diffraction (XRPD). The XRPD patterns for composites reveal the quantities of each original phase present.

The infrared spectra of the samples reinforce this structural verification indicating no or minimal occurrence of unwanted reactions. The first sample (x = 0) and last sample (x = 1) in this series exhibit the maximum and the minimum of the relative dielectric permittivity and values range from 140.1 to 8.3 respectively.

The measured temperature coefficient of the matrix CaTiO3 was +921 ppm·°C-1 and for the matrix Cr3/4Fe5/4O3 was -56 ppm·°C-1. With the study of series of composites, it was possible to make a mathematical prediction for a composition reach the temperature coefficient near zero. The proposed ceramic has potential use as thermostable material in the microwave region and can be applied to resonators, low-noise amplifiers, filters, and so on.

In the research paper of QUANTUM ESPRESSO is an integrated suite of computer codes for electronic-structure calculations and materials modeling, based on density-functional theory, plane waves, and pseudopotentials (norm-conserving, ultrasoft, and projector-augmented wave).

The acronym ESPRESSO stands for open Source Package for Research in Electronic Structure, Simulation, and Optimization. It is freely available to researchers around the world under the terms of the GNU General Public License.

QUANTUM ESPRESSO builds upon newly-restructured electronic-structure codes that have been developed and tested by some of the original authors of novel electronic-structure algorithms and applied in the last twenty years by some of the leading materials modeling groups worldwide.

Innovation and efficiency are still its main focus, with special attention paid to massively parallel architectures, and a great effort being devoted to user friendliness.

QUANTUM ESPRESSO is evolving towards a distribution of independent and interoperable codes in the spirit of an open-source project, where researchers active in the field of electronic-structure calculations are encouraged to participate in the project by contributing their own codes or by implementing their own ideas into existing codes.

In the Research paper Vanderbilt, David had a new approach to the construction of first-principles pseudopotentials is described. The method allows transferability to be improved systematically while holding the cutoff radius fixed, even for large cutoff radii.

Novel features are that the pseudopotential itself becomes charge-state dependent, the usual norm-conservation constraint does not apply, and a generalized eigenproblem is introduced. The potentials have a separable form well suited for plane-wave solid-state calculations, and show promise for application to first-row and transition-metal systems.

In the Research paper Perdew, John P., Kieron Burke, and Matthias Ernzerhof states that Generalized gradient approximations (GGA's) for the exchange-correlation energy improve upon the local spin density (LSD) description of atoms, molecules, and solids.

We present a simple derivation of a simple GGA, in which all parameters (other than those in LSD) are fundamental constants. Only general features of the detailed construction underlying the Perdew-Wang 1991 (PW91) GGA are invoked. Improvements over PW91 include an accurate description of the linear response of the uniform electron gas, correct behavior under uniform scaling, and a smoother potential.

In the Research paper Da Silva, Juarez LF, M. Veronica Ganduglia-Pirovano, Joachim Sauer, Veronika Bayer, and Georg Kresse. periodic density functional theory (DFT) calculations for CeO2 and Ce2O3 using the Perdew-Burke-Ernzerhof (PBE0) and Heyd-Scuseria-Ernzerhof (HSE) hybrid functionals that include nonlocal Fock exchange.

We study structural, electronic, and magnetic ground state properties. Hybrid functionals correctly predict Ce2O3 to be an insulator as opposed to the ferromagnetic metal predicted by the local spin density (LDA) and generalized gradient (GGA) approximations.

The equilibrium volumes of both structures are in very good agreement with experiments, improving upon the description of the LDA and GGA. The calculated CeO2 (O 2p-Ce 5d) and Ce2O3 (Ce 4f-5d4f) band gaps are larger by up to 45% (PBE0) and 15% (HSE) than found in experiments. Furthermore, we calculate atomization energies, heats of formation, and the reduction energy of 2CeO(2)-> Ce2O3+(1/2)O-2. The latter is underestimated by similar to 0.4-0.9 eV with respect to available experimental data at room temperature. We compare our results with the more traditional DFT+U (LDA+U and PBE+U) approach and discuss the role played by the Hubbard U parameter.

In the research paper G. Kresse, "Ab-Initio Molecular-Dynamics for Liquid-Metals," Journal of NonCrystalline Solids, vol. 193, pp. 222-229, Dec 1995. This paper studies the influence of the particle size (with the chosen sizes 2.122 nm; 2.49 nm; 2.884 nm; 3.128 nm; 3.254 nm; 4.07 nm; 4.68 nm; 4.978 nm; 5.3 nm; 6.602 nm; 7.774 nm; 8.392 nm) on the microstructure and the Curie temperature (Tc) of nano-iron particles model.

The nano-iron particles were created by Molecular Dynamics Simulation method with the Pak-Doyama pair interaction potential and a periodic boundary conditions which is called soft boundary or free boundary. The microstructure characteristics were analyzed through the radial distribution function (RDF), the energy and the coordination number. The Curie temperature (T_c) is the point at which materials switch from the ferromagnetic phase to the paramagnetic phase and it is determined through the Using model.

The study purpose of this paper is to determine the relationship between the particle size and the Curie temperature (Tc) of the model. The obtained results showed that there was specific influence of the particle size on the microstructure and the Curie temperature (Tc) of the nano-iron particles model: when the size of the nano-iron particles was increased from 2.122 nm to 2.49 nm; 2.884 nm; 3.128 nm; 3.254 nm; 4.07 nm; 4.68 nm; 4.978 nm; 5.3 nm; 6.602 nm; 7.774 nm; 8.392 nm, the phase transition temperature of the model increased from 8.9 K to 9.3 K; 9.5 K; 9.6 K; 9.7 K K respectively.

The results have also been compared with the results from the theoretical-experimental model showing the significant influence of the particle size on the Curie temperature of the nano-iron particles model. In addition, the nano-iron particles model at different sizes had the different microstructure characteristics and different Curie temperatures.

In the research paper P. F. Manicone, P. Rossi Iommetti, and L. Raffaelli, "An overview of zirconia ceramics: basic properties and clinical applications," Journal of Dentistry, vol. 35, pp. 819-26, 2007. Zirconia (ZrO2) is a ceramic material with adequate mechanical properties for manufacturing of medical devices. Zirconia stabilized with Y2O3 has the best properties for these applications. When a stress occurs on a ZrO2 surface, a crystalline modification opposes the propagation of cracks.

Compression resistance of ZrO2 is about 2000 MPa. Orthopedic research led to this material being proposed for the manufacture of hip head prostheses. Prior to this, zirconia biocompatibility had been studied in vivo; no adverse responses were reported following the insertion of ZrO2 samples into bone or muscle. In vitro experimentation showed absence of mutations and good viability of cells cultured on this material. Zirconia cores for fixed partial dentures (FPD) on anterior and posterior teeth and on implants are now available.

Clinical evaluation of abutments and periodontal tissue must be performed prior to their use. Zirconia opacity is very useful in adverse clinical situations, for example, for masking of dischromic abutment teeth. Radiopacity can aid evaluation during radiographic controls. Zirconia frameworks are realized by using computer-aided design/manufacturing (CAD/CAM) technology.

Cementation of Zr-ceramic restorations can be performed with adhesive luting. Mechanical properties of zirconium oxide FPDs have proved superior to those of other metal-free restorations. Clinical evaluations, which have been ongoing for 3 years, indicate a good success rate for zirconia FPDs. Zirconia implant abutments can also be used to improve the aesthetic outcome of implant-supported rehabilitations. Newly proposed zirconia implants seem to have good biological and mechanical properties; further studies are needed to validate their application.

In the research paper of D. Vanderbilt, "Soft self-consistent pseudopotentials in a generalized eigenvalue formalism," Physical review. B, Condensed matter, vol. 41, pp. 7892-7895, 1990. In this work, we compute the phonon properties of carbon nanotube using finite difference method and DFPT approach separately for comparison. We found that both methods produce very similar phonon frequencies near the G-point.

However, in the high frequency range, the optical phonons from both methods differ significantly. We attribute this difference to the variation of accuracies in atomic force computation in both methods.

In the research paper of Naray-Szabo, S., Zeitschrift fuer Kristallographie, Kristallgeometrie, Kristallphysik, Kristallchemie (-144,1977), 94, 414, (1936).

Atoms shifted by 1/4 0 1/4 to fit space group setting, cp. 26488The structure has been assigned a PDF number (experimental powder diffraction data):37-1484 No R value given in the paper.At least one temperature factor missing in the paper.The coordinates given in the paper contain an error. The values in the database have been corrected.

In the research paper of Faucher, M., Golden Book of Phase Transitions, Wroclaw, 1, 1, (2002). The recent report of an intermediate incommensurately modulated orthorhombic phase in LaTaO4 has prompted a re-examination of the phase transition sequence in LaTaO4 as a function of temperature. With falling temperature, the sequence of phases examined is (orthorhombic) Cmc21(C)↔Cmc21(IC)↔(monoclinic)P21/c, with C and IC denoting commensurate and incommensurate phases, respectively. The orthorhombic to monoclinic transition, Tm−o, is a first order reconstructive transition occurring at 440 K and TIC−C is a first-order displacive transition occurring at 500–530 K. Strain and elasticity data confirm a first-order transition between the basic and modulated Cmc21 phases, with similarities to the isostructural fluoride BaMnF4. A Raman spectroscopic study of the LaTaO4 phase transition indicates that the IC-C phase transition is driven by a soft zone-boundary phonon (unstable) of the commensurate orthorhombic (Cmc21) phase. The soft phonon is found to appear (underdamped) above 443 K and vanishes (overdamped) around 528 K. A large supercell of the monoclinic phase below Tm−o is proposed based on the Raman spectroscopic results.

In the research paper of Dachille, F. Simons, P.Y., Acta Crystallographica (1,1948-23,1967), 23, 334, (1967). Being inherently safe and chemically compatible with the electrolyte, titanium oxide-based materials, including both Li-titanites and various TiO2 polymorphs, are considered alternatives to carbonaceous anodes in Li-ion batteries. Given the commercial success of the spinel lithium titanites, TiO2 polymorphs, in particular in nanostructured forms, have been fabricated and investigated for the applications. Nanostructuring leads to increased reaction areas, shortened Li+ diffusion and potentially enhanced solubility/capacity. Integration with an electron-conductive second phase into the TiO2-based nanostructures eases the electron transport, resulting in further improved lithium electrochemical activity and the overall electrochemical performance. This paper reviews structural characteristics and Li-electrochemical reactivity, along with synthetic approaches, of nanostructures and nano-composites based on lithium titanites and TiO2 polymorphs that include rutile, anatase, bronze and brookite.

In the research paper Williamson GK, Hall WH (1953) X-ray line broadening from filed aluminium and wolfram. Acta Metall Mater 1(1): 22-31. Methods of analysis previously used in the interpretation of line broadening are discussed and are shown to be inadequate; more reliable methods being outlined. An analysis of published results using one of these methods suggests that the observed effects can be attributed to simultaneous small particle size and strain broadening. Measurements of the changes in intensity distribution have been made, using a Geiger counter spectrometer, in the spectra of cold worked aluminium and wolfram. The line breadths may be attributed to simultaneous small particle size and strain broadening, the latter predominating, particularly at the higher Bragg angles, and it is shown that the observed effects are produced by dislocations or some similar structural fault. The observed rise in the breadths of the high angle lines from annealed materials suggests that some dislocations remain after annealing. Fourier analysis of the line shapes in general merely confirm the results of the analysis of the line breadths, but in the case of the recovered specimens it suggests that the dislocations form into walls ("polygonization").

In the research paper Momma K, Izumi F (2011) VESTA 3 for three-dimensional visualization of crystal, volumetric and morphology data. J Appl Crystallogr 44(6):1272-1276.

VESTA is a three-dimensional visualization system for crystallographic studies and electronic state calculations. It has been upgraded to the latest version, *VESTA 3*, implementing new features including drawing the external morphology of crystals; superimposing multiple structural models, volumetric data and crystal faces; calculation of electron and nuclear densities from structure parameters; calculation of Patterson functions from structure parameters or volumetric data; integration of electron and nuclear densities by Voronoi tessellation; visualization of isosurfaces with multiple levels; determination of the best plane for selected atoms; an extended bond-search algorithm to enable more sophisticated searches in complex molecules and cage-like structures; undo and redo in graphical user interface operations; and significant performance improvements in rendering isosurfaces and calculating slices.

CHAPTER 3

COMPUTATIONAL APPROACH OF TBC's

In the Computational approach of TBC's the selected composites are the following:-

1. Amorphous Al_2O_3 doped with Yttria stabilized zirconia
2. Amorphous MoO_3 doped with Yttria stabilized zirconia (YSZ),
3. Pure ZrO2 doped with Yttria stabilized zirconia (YSZ)
4. ZrO2 doped with Yttria stabilized zirconia (YSZ)
5. 7-8YSZ doped with Yttria stabilized zirconia (YSZ)
6. 80%ZrO_2+10%Y_2O_3+10%MoO_3 doped with Yttria stabilized zirconia (YSZ)
7. 80%ZrO_2+10%Y_2O_3+10%Al_2O_3 doped with Yttria stabilized zirconia (YSZ)
8. 90%ZrO_2+5%Y_2O_3+5%Al_2O_3 doped with Yttria stabilized zirconia (YSZ)
9. 90%ZrO_2+5%Y_2O_3+5%TiO_2 doped with Yttria stabilized zirconia (YSZ)
10. 80%ZrO_2+10%Y_2O_3+10%TiO_2 doped with Yttria stabilized zirconia (YSZ)

In this Computational approach can be commutated by Finite Element Analysis Method of heat transfer distribution can observed from layer to layer and to determine the thermal barrier temperatures.

In the Computational approach of TBC's can be theoretically to finding the better performance of Thermal barrier coatings.

The Computational approach can be resolved by COMSOL Multiphysics software are in the field of thermal barrier composites.

The First principle calculations have been performed using the Quantum ESPRESSO PWscf code using a plane-wave basis to express the wave function of the valence electrons and ultrasoft pseudopotentials to describe the interactions of ionic cores and valence electrons . Quantum Wise VNL-ATK 2017 academic version was used as GUI for Quantum ESPRESSO. The exchange-correlation contribution was described by the generalized gradient approximation (GGA) of Perdew, Burke, and Ernzerhof .

Onsite Coulomb correction (GGA + U) was included to describe the localized electronic states of Zr 3d in mixed-valence rare earth metals. A spin polarization calculation was used. A kinetic cut off energy of 520 eV, and 3× 3 × 3 k-point meshes in the unit cell were found by a convergence test (< 3 meV). Because the band gaps of both compounds were underestimated, this is typical of the GGA + U functional . The relaxation of unit cell volume was done by total-energy minimization, and atom positions were relaxed until the remaining force acting on the atoms was less than 10−3 eV/Å. elastic stiffness, the anisotropic Young's modulus on (0 1 1) plane was calculated.

The volume and relative bond ratio as a function of hydrostatic pressure were also computed. Study of the thermal properties of different phases of zirconia has been reported. All experimentally measured the specific heat capacity at constant volume. They investigated the thermal properties of pure zirconia and YSZ by adiabatic calorimetry measurement at a temperature range between 13 K and 300 K. Several attempts were made to investigate the properties and the phase transition nature of zirconia [6, 7] using density functional theory (DFT). Lou et al investigated the thermodynamic properties and temperature based monoclinic to tetragonal phase transition for both ZrO2 and HfO2 using ab initio method. The temperature dependency of heat capacity of two materials was validated. The Computational studies will focus on the thermodynamic properties of monoclinic zirconia, and investigate the pressure-dependent structure of tetragonal zirconia, and tetragonal zirconia transformation under hydrostatic compressive pressures.

Applications of TBC's:

A thermal barrier is a material that is applied between spray foam insulation and the interior living space. The thermal barrier is used mostly as **a fire resistance measure**.

Thermal barrier coatings (TBCs) are widely applied in **protecting metallic components**, which are used in aero- and land-based gas turbines. These hot-section components include a combustion chamber, blades, and vanes. The TBC leads to significant reduction of heat transfer from the high temperature gas to metal surface.

A thermal barrier coating (TBC) is a highly advanced system applied to surfaces, like metals, especially in **aviation engine and gas turbine parts** that operate at extremely high temperatures. It performs well in managing exhaust heat.

At present, the commonly used thermal barrier coating ceramic materials are mainly **Al_2O_3, SiO_2, ZrO_2**, wherein zirconia ceramics have a high melting point and low thermal conductivity, and the thermal expansion coefficient is close to that of metal materials, and is widely used as a ceramic material for thermal barrier Coatings.

The most commonly applied TBC material is yttria stabilized zirconia (YSZ) which exhibits resistance to thermal shock and thermal fatigue up to 1150°C. YSZ is generally deposited by **plasma spraying and electron** beam physical vapour deposition (EBPVD) processes.

Process of TBC's :

Formation of a dense, continuous, slow-growing alumina layer (TGO) between a ceramic top coat and an underlying bond coat during service influences the lifetime of the TBC systems. During thermal treatment at 1,100°C in air, the amorphous oxide layer transforms to α-Al_2O_3 in the as-deposited samples.
Barrier coatings **protect from corrosion by preventing external elements from penetrating to the substrate via a plastic resin layer**. Sacrificial coatings contain certain elements, such as zinc or aluminum, which corrode sacrificially to ensure that the component's substrate remains corrosion free.

Overview of TBC's :

Thermal barrier coatings (TBCs) are widely applied in protecting metallic components, which are used in aero- and land-based gas turbines. These hot-section components include a combustion chamber, blades, and vanes. The TBC **leads to significant reduction of heat transfer from the high temperature gas to metal surface**.

Definition of TBC's

A limit to unlimited increase in airplane or rocket speeds imposed by aerodynamic heating that without adequate provisions for cooling the exposed surfaces will result in loss of strength and eventual melting of the metal skin. It is also called heat barrier.

Modules of Thermal barrier composites in COMSOL software:

It shows how to set up multiple sandwiched thin layers with different thermal conductivities in two different ways. First, the composite is modeled as a 3D object. In the second approach the Thin Layer boundary condition with the thermally thick option

is used to avoid resolving the thin domains. The technique is useful when modeling heat transfer through thermal barriers like multilayer coatings.

CHAPTER 4

MATERIALS AND METHODS USED

INTRODUCTION

This chapter deals with the procedures followed for selection of compositions, sample preparation, glass formation and crystallization of the glass network. It also describes the various experimental techniques and DFT Calculations are employed in the characterization of glass and glass ceramics used for TBC coating. The apparatus used and detailed procedures followed in studying XRD and DFT calculations are described. The various steps involved in the formation of TBC materials and characterization techniques, DFT methods employed on the synthesized glass ceramic sample is represented as a flowchart in Figure 3.1.

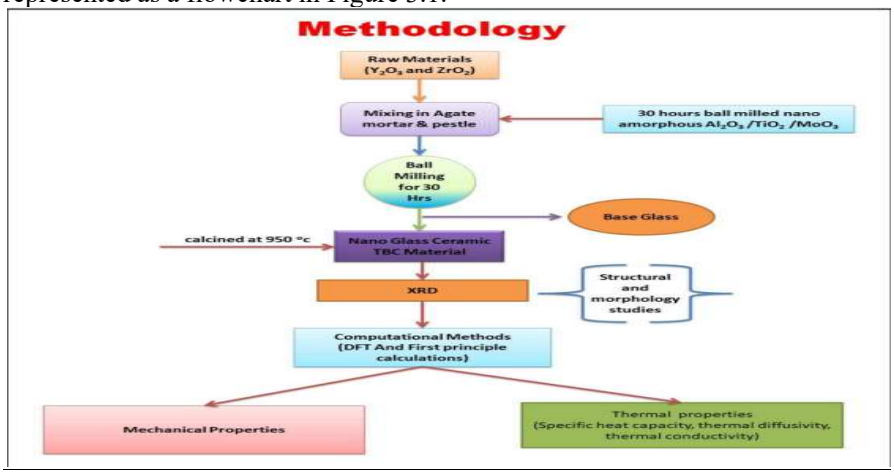

Figure 4.1: Flow Chart illustrating the entire process of glass and glass ceramic fabrication and characterization for TBC.

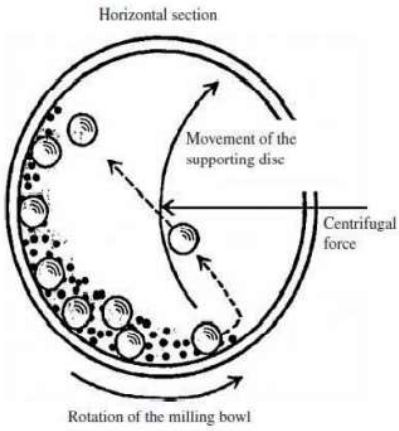

4.2 GLASS AND GLASS CERAMIC SAMPLE PREPARATION VIA HIGH ENERGY PLANETARY BALL MILLING TECHNIQUE

Several cost-effective techniques have been proposed to produce fine powders from very fine to nanoscale with desirable performance in the literature (Kang et al., 2003; Xu and Gao, 2004; Lam et al., 2004; Suzuki and Kijima, 2004; Dell et al., 2007). In particular, high energy planetary ball milling technique is simple and efficient for the large-scale production of nanoscaled powders as well as to achieve a close contact between electrodes and electrolyte which we have been used for the present study (Suryanarayana, 2001). The high energy planetary ball mill equipped with the planet-like movement of its vials,

arranged in a rotating support disk. These vials are rotated around their own axes following the principle of centrifugal acceleration (Figure 2.1). The charge inside vials claims two relative motions: a rotary motion around the mill axis and a planetary motion around the vial axis (Figure 2.2). Figure 2.3: Movements of working parts and balls in a planetary mill Figure 2.2: High energy planetary mill 8 The vials are partially fed with the precursor material whose particle size is to be reduced. As a result of the milling process, the balls rotate with high speed inside the vials and the powder experiences a gravitational force. This in turn, plastically deforms the bulk powder particles into a finer or nanoscale powder, depending upon the milling duration (Figure 2.3). 2.3 Sample Characterization The degree of nanocrystalline phases of the synthesized glass ceramics was checked by the X-ray diffraction analysis recorded using PANalytical Diffractometer B.V fitted with copper target and nickel filter operated at 40 kV, 30 mA.

4.4 CHARACTERIZATION TECHNIQUES

3.4.1 X-ray Powder Diffraction XRD is a standard characterization technique to obtain structural details (crystal structure, lattice parameters, disorder, defects, and crystallinity of bulk and nanocrystalline materials. In general, sharp peaks with high intensity reflect the crystalline nature of the compound. A short-range atomic order and absence of diffraction peaks reveals the glassy nature, whereas broad and diffused peaks would reflect the glass ceramic nature.

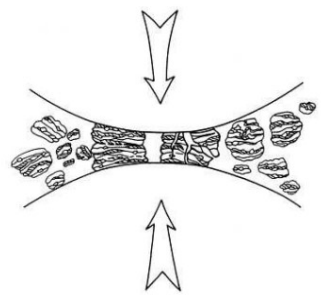

Figure 4.4: Ball-Powder-ball collision of powder mixture during mechanical alloying.

9 The positions of the diffraction peaks in XRD pattern follow the well-known Bragg's law

$$2d_{hkl} \sin\theta = n\lambda \quad (3.1)$$

Where 'λ' is the X-ray wavelength, 'dhkl' is the spacing between crystallographic planes giving rise to a particular diffracted beam, 'θ' is the incidence angle and 'n' is an integer which represents the order of diffraction peaks as shown in Figure 4.5

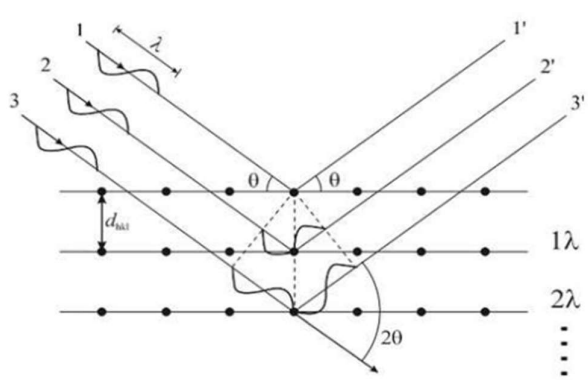

Figure4 .5: Schematic view of X-ray diffraction

Crystallinity can be obtained by the comparison of background pattern intensity with the sharp peaks. Figure 4.6 Broadening of XRD pattern Figure 4.6: Broadening of XRD Pattern The broad

intensified peaks will be recorded for crystallites of smaller size (Figure 4.6), which can be estimated from the Scherer's formula (Suryanarayana, 2001). (4.2) Where d is the crystallite size, λ is the wavelength of the X-ray radiation used, 'θ' is the angle of diffraction and 'β' is the full width (in radian) at the half-maximum intensity. The photograph of PHILIPS X'Pert X-ray diffractometer is shown in Figure 4.7

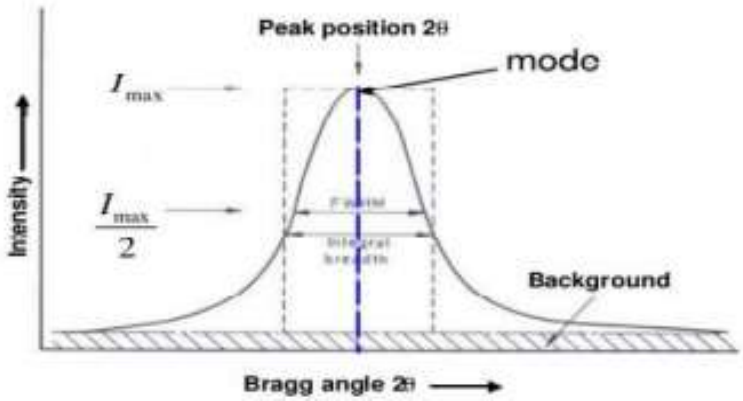

Figure 4.6 Broadening of XRD pattern

Figure 4.7: Photograph of PHILIPS X'Pert X-ray diffractometer

Applications of X-Ray diffraction method :

X-ray powder diffraction is most widely used for the **identification of unknown crystalline materials** (e.g. minerals, inorganic compounds). Determination of unknown solids is critical to studies in geology, environmental science, material science, engineering and biology.

Advantages of X-Ray diffraction method :

- It is a rapid and powerful technique for identifying unknown minerals and materials.
- It only requires preparation of a minimal sample for analysis.
- Interpreting the resulting data is relatively straightforward.
- XRD measurement instruments are widely available.

CHAPTER 5

COMPUTATION OF TBC's ON STEEL SURFACE

In the Computational methods for finding the best Thermal Barrier Coatings among the characteristics such as thermal conductivity, thermal barrier temperatures among the test composite TBC's such as

- Amorphous Al_2O_3 doped with Yttria stabilized zirconia ,
- Amorphous MoO_3 doped with Yttria stabilized zirconia (YSZ),
- Pure ZrO_2 doped with Yttria stabilized zirconia (YSZ),
- ZrO_2 doped with Yttria stabilized zirconia (YSZ),
- 7-8YSZ doped with Yttria stabilized zirconia (YSZ),
- 80%ZrO_2+10%Y_2O_3+10%MoO_3 doped with Yttria stabilized zirconia (YSZ),
- 90%ZrO_2+5%Y_2O_3+5%MoO_3 doped with Yttria stabilized zirconia (YSZ) ,
- 80%ZrO_2+10%Y_2O_3+10%Al_2O_3 doped with Yttria stabilized zirconia (YSZ),
- 90%ZrO_2+5%Y_2O_3+5%Al_2O_3 doped with Yttria stabilized zirconia (YSZ),
- 90%ZrO_2+5%Y_2O_3+5%TiO_2 doped with Yttria stabilized zirconia (YSZ),
- 80%ZrO_2+10%Y_2O_3+10%TiO_2 doped with Yttria stabilized zirconia (YSZ).

In the above thermal barrier composites modules will be computed by the following

First, the composite is modeled as a 3D object.

In the second approach the Thin Layer boundary condition is used to avoid resolving the thin domains.

These are the following contents :-

- Global Definitions
- 1.1. Parameters
- 1.2. Materials
- 2. Component 1
- 2.1. Definitions

Computational approach Performance of 7-8 YSZ :

Global Definitions:

Global settings

Name	7-8 YSZ doped YSZ.mph
Path	C:\Users\sivam\OneDrive\Desktop\TBC mph files\7-8 YSZ doped YSZ.mph
Version	COMSOL Multiphysics 5.6 (Build: 401)
Unit system	SI

Used products

COMSOL Multiphysics
Heat Transfer Module

Computer information

CPU	Intel64 Family 6 Model 142 Stepping 10, 2 cores
Operating system	Windows 10

Fig 5.1 table for global definitions

5.1.1. Parameters

Parameters 1

Name	Expression	Value	Description
d_YSZ	50[um]	5E−5 m	Thickness of layer 1
d_7to8YSZ	75[um]	7.5E−5 m	Thickness of layer 2
T_hot	1220[degC]	1493.2 K	Hot temperature

Fig 5.2 table for Parameters of layer thickness and temperature

5.1.2. Materials

1.2.1. Steel AISI 4340

Material parameters

Name	Value	Unit
Heat capacity at constant pressure	475[J/(kg*K)]	J/(kg·K)
Density	7850[kg/m^3]	kg/m³
Thermal conductivity	44.5[W/(m*K)]	W/(m·K)

Basic

Description	Value
Relative permeability	{{1, 0, 0}, {0, 1, 0}, {0, 0, 1}}
relpermeability_symmetry	3
Electrical conductivity	{{4.032e6[S/m], 0, 0}, {0, 4.032e6[S/m], 0}, {0, 0, 4.032e6[S/m]}}
electricconductivity_symmetry	3
Coefficient of thermal expansion	{{12.3e-6[1/K], 0, 0}, {0, 12.3e-6[1/K], 0}, {0, 0, 12.3e-6[1/K]}}
thermalexpansioncoefficient_symmetry	3
Heat capacity at constant pressure	475[J/(kg*K)]
heatcapacity_symmetry	0
Relative permittivity	{{1, 0, 0}, {0, 1, 0}, {0, 0, 1}}
relpermittivity_symmetry	3
Density	7850[kg/m^3]
density_symmetry	0
Thermal conductivity	{{44.5[W/(m*K)], 0, 0}, {0, 44.5[W/(m*K)], 0}, {0, 0, 44.5[W/(m*K)]}}
thermalconductivity_symmetry	3

Young's modulus and Poisson's ratio

Description	Value
Young's modulus	205e9[Pa]
youngsmodulus_symmetry	0
Poisson's ratio	0.28
poissonsratio_symmetry	0

Fig 5.3 Table for Materials parameters and their properties

1.2.2. Ceramic 1

Material parameters

Name	Value	Unit
Thermal conductivity	1	W/(m·K)
Density	6000	kg/m³
Heat capacity at constant pressure	320	J/(kg·K)

Fig 5.4 Table for Materials parameters in Ceramic 1

- Thermal conductivity ={{1, 0, 0}, {0, 1, 0}, {0, 0, 1}}
- Thermalconductivity_symmetry = 0
- Density =6000
- density_symmetry = 0
- Heat capacity at constant pressure =320
- heatcapacity_symmetry = 0

5. 1.2.3. 7-8YSZ

Material parameters

Name	Value	Unit
Thermal conductivity	0.5	W/(m·K)
Density	2200	kg/m³
Heat capacity at constant pressure	425	J/(kg·K)

Basic

Description	Value
Thermal conductivity	{{0.5, 0, 0}, {0, 0.5, 0}, {0, 0, 0.5}}
thermalconductivity_symmetry	0
Density	2200
density_symmetry	0
Heat capacity at constant pressure	425
heatcapacity_symmetry	0

Fig 5.5 Table for Materials parameters and their properties of 7-8 YSZ

5.1.2.4. Layered Material 1

5.2. Component 1

Settings

Description	Value
Unit system	Same as global system (SI)
Geometry shape function	Automatic

Spatial frame coordinates

First	Second	Third
x	y	z

Material frame coordinates

First	Second	Third
X	Y	Z

Geometry frame coordinates

First	Second	Third
Xg	Yg	Zg

Mesh frame coordinates

First	Second	Third
Xm	Ym	Zm

Fig 5.6 Table for Layered Material in Component 1

2.1. Definitions

2.1.1. Variables

Variables: temperature in thermal barrier

Selection

Geometric entity level	Entire model

Name	Expression	Unit	Description
vol_barrier	intopBarrier(1)	m³	Volume of barrier
vol_layer1	intopLayer1(1)	m³	Volume of layer 1
vol_layer2	intopLayer2(1)	m³	Volume of layer 2
T_int_barrier	intopBarrier(T)	m³·K	Integral of temperature in thermal barrier
T_int_layer1	intopLayer1(T)	m³·K	Integral of temperature in layer 1
T_int_layer2	intopLayer2(T)	m³·K	Integral of temperature in layer 2
T_ave_barrier	intopBarrier(T)/intopBarrier(1)	K	Average of temperature in thermal barrier
T_ave_layer1	intopLayer1(T)/intopLayer1(1)	K	Average of temperature in layer 1
T_ave_layer2	intopLayer2(T)/intopLayer2(1)	K	Average of temperature in layer 2

Fig 5.7 Table for selection of variables

2.1.2. Nonlocal Couplings

Integration : Barrier

Coupling type	Integration
Operator name	intopBarrier

Selection

Geometric entity level	Domain
Selection	Geometry geom1: Dimension 3: Domains 2–3

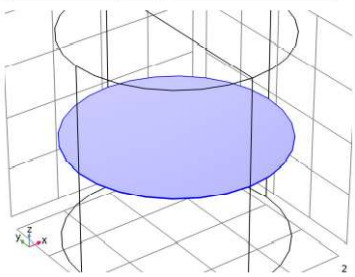

Selection

Fig 5.8 Selection of the Entity level domain in layer barrier

Integration : Layer 1

Coupling type	Integration
Operator name	intopLayer1

Selection

Geometric entity level	Domain
Selection	Geometry geom1: Dimension 3: Domain 2

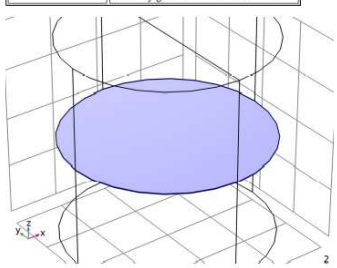

Selection

Fig 5.9 Selection of the Entity level domain in layer 1

Integration : Layer 2

Coupling type	Integration
Operator name	intopLayer2

Selection

Geometric entity level	Domain
Selection	Geometry geom1: Dimension 3: Domain 3

Fig 5.1.1 Table for Selection of the Entity level domain in layer 2

2.1.3. Coordinate Systems

Boundary System 1

Coordinate system type	Boundary system
Tag	sys1

Coordinate names

First	Second	Third
t1	t2	n

Fig 5.1.2 Table for Selection of the Entity level domain in Boundary System

2.2. Geometry 1

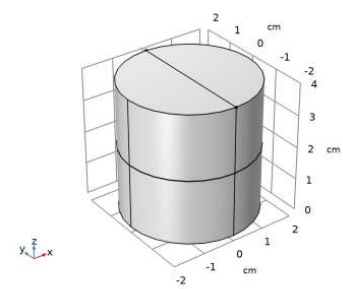

Fig 5.1.2 Selection of the Entity level domain in Geometry 1

Units

Length unit	cm
Angular unit	deg

Geometry statistics

Description	Value
Space dimension	3
Number of domains	4
Number of boundaries	22
Number of edges	37
Number of vertices	20

Fig 5.1.3 Table for Selection of the Entity level domain in Geometry 1

5.2.2.1. Cylinder 1 (cyl1)

Position

Description	Value
Position	{0, 0, 0}

Fig 5.1.4 Table for Selection of the position in Cylinder 1

Axis

Description	Value
Axis type	z – axis

Fig 5.1.5 Table for Selection of the axis in Cylinder 1

Size and shape

SlNo.	Description	Value
1	Radius	2
2	Height	4

Fig 5.1.6 Table for Selection of the size and shape in Cylinder 1

2.2.2. Cylinder 2 (cyl2)

Position

Description	Value
Position	{0, 0, 2 - (d_YSZ + d_7to8YSZ)/2}

Axis

Description	Value
Axis type	z - axis

Size and shape

Description	Value
Radius	2
Height	d_YSZ

Fig 5.1.7 Table for Selection of the position in Cylinder 2

2.2.3. Cylinder 3 (cyl3)

Position

Description	Value
Position	{0, 0, 2 - (d_7to8YSZ + d_7to8YSZ)/2 + d_YSZ}

Axis

Description	Value
Axis type	z - axis

Size and shape

Description	Value
Radius	2
Height	d_7to8YSZ

Fig 5.1.8 Table for Selection of the position in Cylinder 3

2.2.4. Polygon 1 (pol1)

Object type

Description	Value
Type	Open curve

Coordinates

Description	Value
Data source	Table

Coordinates

x (cm)	y (cm)	z (cm)
0	-2	4
0	2	4

Fig 5.1.9 Table for Selection of the coordinates in Polygon 1

5.2.3. Materials

5.2.3.1. Material Link 1

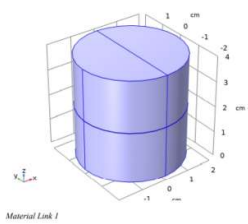

Fig 5.1.9.1 fig. of Selection of the Material link 1

Selection

Geometric entity level	Domain
Selection	Geometry geom1: Dimension 3: All domains

Fig 5.2.0 Table for Selection of the position in Geometry for Material link 1

2.3.2. Material Link 2

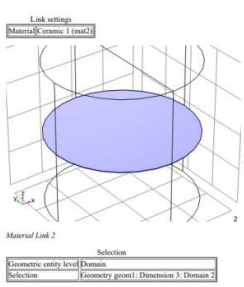

Fig 5.2.1 Selection of the position in Mat. Link 2

2.3.3. Material Link 3

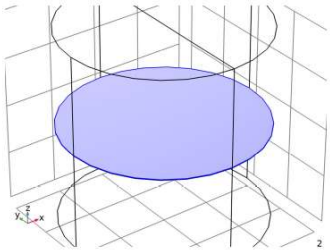

Material Link 3

Selection

Geometric entity level	Domain
Selection	Geometry geom1: Dimension 3: Domain 3

Fig 5.2.2 Selection of the position in Material link 3

5.2.4. Heat Transfer in Solids

Used products

COMSOL Multiphysics

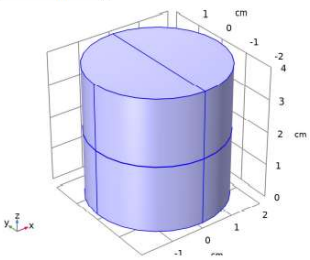

Heat Transfer in Solids

Selection

Geometric entity level	Domain
Selection	Geometry geom1: Dimension 3: All domains

Equations

$$\rho C_p \mathbf{u} \cdot \nabla T + \nabla \cdot \mathbf{q} = Q + Q_{ted}$$

$$\mathbf{q} = -k\nabla T$$

Fig 5.2.3 for Selection of the heat transfer in solids in Cylinder

2.4.1. Interface Settings

Discretization

Settings

Description	Value
Temperature	Quadratic Lagrange

Physical Model

Settings

Description	Value
Isothermal domain	Off
Reference temperature	User defined
Reference temperature	293.15[K]

Fig 5.2.4 Table for Setting of Interface in discretization

2.4.2. Variables

Name	Expression	Unit	Description	Region	Meta
ht.Tref	model.input.Tref	K	Reference temperature	Global	
ht.d	1	1	Thickness	Domains 1–4	
ht.HRef	0	J/kg	Reference enthalpy	Domains 1–4	
ht.alphap	0	1/K	Isobaric compressibility coefficient	Domains 1–4	
ht.DeltaH	0	J/kg	Sensible enthalpy	Domains 1–4	+ operatio
ht.H	0	J/kg	Enthalpy	Domains 1–4	+ operatio
ht.H0	ht.H+ht.Ek	J/kg	Total enthalpy	Domains 1–4	
ht.Ei	0	J/kg	Internal energy	Domains 1–4	+ operatio
ht.Ei0	ht.Ei+ht.Ek	J/kg	Total internal energy	Domains 1–4	
ht.Ek	0	J/kg	Kinetic energy	Domains 1–4	+ operatio
ht.dfluxx	0	W/m²	Conductive heat flux, x component	Domains 1–4	+ operatio
ht.dfluxy	0	W/m²	Conductive heat flux, y component	Domains 1–4	+ operatio
ht.dfluxz	0	W/m²	Conductive heat flux, z component	Domains 1–4	+ operatio
ht.dfluxx	mean(ht.dfluxx)	W/m²	Conductive heat flux, x component	Boundaries 1–22	+ operatio
ht.dfluxy	mean(ht.dfluxy)	W/m²	Conductive heat flux, y component	Boundaries 1–22	+ operatio
ht.dfluxz	mean(ht.dfluxz)	W/m²	Conductive heat flux, z component	Boundaries 1–22	+ operatio
ht.dfluxtestx	0	W/m²	Conductive heat flux, x component	Domains 1–4	+ operatio
ht.dfluxtesty	0	W/m²	Conductive heat flux, y component	Domains 1–4	+ operatio
ht.dfluxtestz	0	W/m²	Conductive heat flux, z component	Domains 1–4	+ operatio
ht.dfluxtestx	mean(ht.dfluxtestx)	W/m²	Conductive heat flux, x component	Boundaries 1–22	+ operatio
ht.dfluxtesty	mean(ht.dfluxtesty)	W/m²	Conductive heat flux, y component	Boundaries 1–22	+ operatio
ht.dfluxtestz	mean(ht.dfluxtestz)	W/m²	Conductive heat flux, z component	Boundaries 1–22	+ operatio
ht.dfluxMag	sqrt(ht.dfluxx^2+ht.dfluxy^2+ht.dfluxz^2)	W/m²	Conductive heat flux magnitude	Domains 1–4	
ht.cfluxx	0	W/m²	Convective heat flux, x component	Domains 1–4	+ operatio
ht.cfluxy	0	W/m²	Convective heat flux, y component	Domains 1–4	+ operatio
ht.cfluxz	0	W/m²	Convective heat flux, z component	Domains 1–4	+ operatio
ht.cfluxMag	sqrt(ht.cfluxx^2+ht.cfluxy^2+ht.cfluxz^2)	W/m²	Convective heat flux magnitude	Domains 1–4	
ht.tfluxx	ht.dfluxx+ht.cfluxx	W/m²	Total heat flux, x component	Domains 1–4	
ht.tfluxy	ht.dfluxy+ht.cfluxy	W/m²	Total heat flux, y component	Domains 1–4	
ht.tfluxz	ht.dfluxz+ht.cfluxz	W/m²	Total heat flux, z component	Domains 1–4	

Fig 5.2.5 Table for Selection of the variables iteration 1

ht.dfluxtestz	mean(ht.dfluxtestz)	W/m²	Conductive heat flux, z component	Boundaries 1–22	+ operation
ht.dfluxMag	sqrt(ht.dfluxx^2+ht.dfluxy^2+ht.dfluxz^2)	W/m²	Conductive heat flux magnitude	Domains 1–4	
ht.cfluxx	0	W/m²	Convective heat flux, x component	Domains 1–4	+ operation
ht.cfluxy	0	W/m²	Convective heat flux, y component	Domains 1–4	+ operation
ht.cfluxz	0	W/m²	Convective heat flux, z component	Domains 1–4	+ operation
ht.cfluxMag	sqrt(ht.cfluxx^2+ht.cfluxy^2+ht.cfluxz^2)	W/m²	Convective heat flux magnitude	Domains 1–4	
ht.tfluxx	ht.dfluxx+ht.cfluxx	W/m²	Total heat flux, x component	Domains 1–4	
ht.tfluxy	ht.dfluxy+ht.cfluxy	W/m²	Total heat flux, y component	Domains 1–4	
ht.tfluxz	ht.dfluxz+ht.cfluxz	W/m²	Total heat flux, z component	Domains 1–4	
ht.tfluxMag	sqrt(ht.tfluxx^2+ht.tfluxy^2+ht.tfluxz^2)	W/m²	Total heat flux magnitude	Domains 1–4	
ht.tefluxx	0	W/m²	Total energy flux, x component	Domains 1–4	+ operation
ht.tefluxy	0	W/m²	Total energy flux, y component	Domains 1–4	+ operation
ht.tefluxz	0	W/m²	Total energy flux, z component	Domains 1–4	+ operation
ht.tefluxMag	sqrt(ht.tefluxx^2+ht.tefluxy^2+ht.tefluxz^2)	W/m²	Total energy flux magnitude	Domains 1–4	
ht.thfluxx	0	W/m²	Total enthalpy flux, x component	Domains 1–4	+ operation
ht.thfluxy	0	W/m²	Total enthalpy flux, y component	Domains 1–4	+ operation
ht.thfluxz	0	W/m²	Total enthalpy flux, z component	Domains 1–4	+ operation
ht.thfluxMag	sqrt(ht.thfluxx^2+ht.thfluxy^2+ht.thfluxz^2)	W/m²	Total enthalpy flux magnitude	Domains 1–4	
ht.dflux_ux	up(ht.dfluxx)	W/m²	Conductive heat flux, x component	Boundaries 1–22	

Fig 5.2.6 Table for Selection of the variables iteration 2

ht.dflux_uy	up(ht.dfluxy)	W/m²	Conductive heat flux, y component	Boundaries 1–22	
ht.dflux_uz	up(ht.dfluxz)	W/m²	Conductive heat flux, z component	Boundaries 1–22	
ht.dflux_dx	down(ht.dfluxx)	W/m²	Conductive heat flux, x component	Boundaries 1–22	
ht.dflux_dy	down(ht.dfluxy)	W/m²	Conductive heat flux, y component	Boundaries 1–22	
ht.dflux_dz	down(ht.dfluxz)	W/m²	Conductive heat flux, z component	Boundaries 1–22	
ht.dfluxtest_ux	up(ht.dfluxtestx)	W/m²	Conductive heat flux, x component	Boundaries 1–22	
ht.dfluxtest_uy	up(ht.dfluxtesty)	W/m²	Conductive heat flux, y component	Boundaries 1–22	
ht.dfluxtest_uz	up(ht.dfluxtestz)	W/m²	Conductive heat flux, z component	Boundaries 1–22	
ht.dfluxtest_dx	down(ht.dfluxtestx)	W/m²	Conductive heat flux, x component	Boundaries 1–22	
ht.dfluxtest_dy	down(ht.dfluxtesty)	W/m²	Conductive heat flux, y component	Boundaries 1–22	
ht.dfluxtest_dz	down(ht.dfluxtestz)	W/m²	Conductive heat flux, z component	Boundaries 1–22	
ht.rflux	0	W/m²	Radiative heat flux	Boundaries 1–22	+ operation
ht.nflux	mean(ht.cfluxx)*ht.nxmesh+mean(ht.cfluxy)*ht.nymesh+mean(ht.cfluxz)*ht.nzmesh	W/m²	Normal convective heat flux	Boundaries 1–22	
ht.nflux_u	up(ht.cfluxx)*ht.nxmesh+up(ht.cfluxy)*ht.nymesh+up(ht.cfluxz)*ht.nzmesh	W/m²	Internal normal convective heat flux, upside	Boundaries 1–22	
ht.nflux_d	down(ht.cfluxx)*ht.nxmesh+down(ht.cfluxy)*ht.nymesh+down(ht.cfluxz)*ht.nzmesh	W/m²	Internal normal convective heat flux, downside	Boundaries 1–22	
ht.nflux	0.5*(ht.nflux_d-ht.nflux_u)	W/m²	Normal convective heat flux	Boundaries 1–22	+ operation
ht.nflux_u	-ht.nflux_d	W/m²	Internal normal convective heat flux, upside	Boundaries 1–5, 7–8, 10–11, 13–22	+ operation
ht.nflux_u	0	W/m²	Internal normal convective heat flux, upside	Boundaries 6, 9, 12	+ operation
ht.nflux_d	0	W/m²	Internal normal convective heat flux, downside	Boundaries 1–22	+ operation
ht.nflux	ht.nflux+ht.nflux	W/m²	Normal total heat flux	Boundaries 1–22	
ht.nflux_u	ht.nflux_u+ht.nflux_u	W/m²	Internal normal total heat flux, upside	Boundaries 1–22	
ht.nflux_d	ht.nflux_d+ht.nflux_d	W/m²	Internal normal total heat flux, downside	Boundaries 1–22	
ht.nrflux	mean(ht.rflux)*ht.nxmesh+mean(ht.rflux)*ht.nymesh+mean(ht.rflux)*ht.nzmesh-mean(ht.dflux)*ht.nxmesh-mean(ht.dflux)*ht.nymesh-mean(ht.dflux)*ht.nzmesh+ht.nflux	W/m²	Normal total energy flux	Boundaries 1–22	
ht.nrflux_u	up(ht.rflux)*ht.nxmesh+up(ht.rflux)*ht.nymesh+up(ht.rflux)*ht.nzmesh-up(ht.dflux)*ht.nxmesh-up(ht.dflux)*ht.nymesh-up(ht.dflux)*ht.nzmesh+ht.nflux_u	W/m²	Internal normal total energy flux, upside	Boundaries 1–22	
ht.nrflux_d	down(ht.rflux)*ht.nxmesh+down(ht.rflux)*ht.nymesh+down(ht.rflux)*ht.nzmesh-down(ht.dflux)*ht.nxmesh-down(ht.dflux)*ht.nymesh-down(ht.dflux)*ht.nzmesh+ht.nflux_d	W/m²	Internal normal total energy flux, downside	Boundaries 1–22	
ht.nhflux	mean(ht.hflux)*ht.nxmesh+mean(ht.hflux)*ht.nymesh+mean(ht.hflux)*ht.nzmesh	W/m²	Normal total enthalpy flux	Boundaries 1–22	
ht.nhflux_u	up(ht.hflux)*ht.nxmesh+up(ht.hflux)*ht.nymesh+up(ht.hflux)*ht.nzmesh	W/m²	Internal normal total enthalpy flux, upside	Boundaries 1–22	
ht.nhflux_d	down(ht.hflux)*ht.nxmesh+down(ht.hflux)*ht.nymesh+down(ht.hflux)*ht.nzmesh	W/m²	Internal normal total enthalpy flux, downside	Boundaries 1–22	
ht.Qm	0	kg/(m³·s)	Mass source	Domains 1–4	
ht.Q	0	W/m³	Heat source	Domains 1–4	+ operation
ht.Qexp	0	W/m³	Out-of-plane heat source	Domains 1–4	+ operation
ht.Qtot	0	W/m³	Total heat source	Domains 1–4	+ operation
ht.Qbnd	0	W/m³	Total boundary heat source	Boundaries 1–22	+ operation
ht.nflux_constr	0	W/m²	Boundary sources and fluxes contribution	Domains 1–4	+ operation
ht.Qtot	0	W/m³	Total interior source	Domains 1–4	+ operation
ht.qs	0	W/(m³·K)	Out-of-plane heat coefficient	Domains 1–4	+ operation
ht.qs_exp	0	W/(m³·K)	Out-of-plane production/absorption coefficient	Domains 1–4	+ operation
ht.Qfint	0	W/m	Total line heat source	Edges 1–37	+ operation

Fig 5.2.7 Table for Selection of the variable iteration 3

ht.Qlrtot	0	W/m	Total line heat source with radius	Edges 1–37	+ operation
ht.Qprtot	0	W	Total point heat source	Points 1–20	+ operation
ht.Qprtot	0	W	Total point heat source with radius	Points 1–20	+ operation
ht.Tvar	T	K	Temperature	Domains 1–4	
ht.Tvar	T	K	Temperature	Boundaries 1–22	
ht.Tvar	T	K	Temperature	Edges 1–37	
ht.Tvar	T	K	Temperature	Points 1–20	
ht.Tu	up(T)	K	Temperature	Boundaries 6, 9, 12	
ht.Tu	T	K	Temperature	Boundaries 1–5, 7–8, 10–11, 13–22	
ht.Td	down(T)	K	Temperature	Boundaries 6, 9, 12	
ht.Td	T	K	Temperature	Boundaries 1–5, 7–8, 10–11, 13–22	
ht.du	up(ht.d)	1	Thickness	Boundaries 6, 9, 12	
ht.du	ht.d	1	Thickness	Boundaries 1–5, 7–8, 10–11, 13–22	
ht.dd	down(ht.d)	1	Thickness	Boundaries 6, 9, 12	
ht.dd	ht.d	1	Thickness	Boundaries 1–5, 7–8, 10–11, 13–22	
ht.q0	0	W/m²	Inward heat flux	Boundaries 1–5, 7–8, 10–11, 13–22	+ operation
ht.nx	nx	1	Normal vector, x component	Boundaries 6, 9, 12	
ht.ny	ny	1	Normal vector, y component	Boundaries 6, 9, 12	
ht.nz	nz	1	Normal vector, z component	Boundaries 6, 9, 12	
ht.nx	dnx	1	Normal vector, x component	Boundaries 1–5, 7–8, 10–11, 13–22	
ht.ny	dny	1	Normal vector, y component	Boundaries 1–5, 7–8, 10–11, 13–22	
ht.nz	dnz	1	Normal vector, z component	Boundaries 1–5, 7–8, 10–11, 13–22	
ht.nxmesh	nxmesh	1	Normal vector (mesh), x component	Boundaries 6, 9, 12	
ht.nymesh	nymesh	1	Normal vector (mesh), y component	Boundaries 6, 9, 12	
ht.nzmesh	nzmesh	1	Normal vector (mesh), z component	Boundaries 6, 9, 12	
ht.nxmesh	dnxmesh	1	Normal vector (mesh), x component	Boundaries 1–5, 7–8, 10–11, 13–22	
ht.nymesh	dnymesh	1	Normal vector (mesh), y component	Boundaries 1–5, 7–8, 10–11, 13–22	
ht.nzmesh	dnzmesh	1	Normal vector (mesh), z component	Boundaries 1–5, 7–8, 10–11, 13–22	
ht.dnx	dnx	1	Normal vector down direction, x component	Boundaries 1–22	
ht.dny	dny	1	Normal vector down direction, y component	Boundaries 1–22	
ht.dnz	dnz	1	Normal vector down direction, z component	Boundaries 1–22	
ht.dnxmesh	dnxmesh	1	Normal vector down direction (mesh), x component	Boundaries 1–22	
ht.dnymesh	dnymesh	1	Normal vector down direction (mesh), y component	Boundaries 1–22	

Fig 5.2.8 Table for Selection of the variable iteration 4

ht.dnzmesh	dnzmesh	1	Normal vector down direction (mesh), z component	Boundaries 1–22	
ht.unx	unx	1	Normal vector up direction, x component	Boundaries 1–22	
ht.uny	uny	1	Normal vector up direction, y component	Boundaries 1–22	
ht.unz	unz	1	Normal vector up direction, z component	Boundaries 1–22	
ht.unxmesh	unxmesh	1	Normal vector up direction (mesh), x component	Boundaries 1–22	
ht.unymesh	unymesh	1	Normal vector up direction (mesh), y component	Boundaries 1–22	
ht.unzmesh	unzmesh	1	Normal vector up direction (mesh), z component	Boundaries 1–22	
ht.dEilnt	0	W	Total accumulated heat rate	Global	+ operation
ht.dE#0Int	0	W	Total accumulated energy rate	Global	+ operation
ht.ntfluxInt	ht.intExtBnd(ht.ntflux*ht.varIntSpa)+ht.intIntBnd(ht.ncflux_u*up(ht.varIntSpa)+ht.ncflux_d*down(ht.varIntSpa))	W	Total net heat rate	Global	
ht.nteffluxInt	ht.intExtBnd(ht.nteflux*ht.varIntSpa)+ht.intIntBnd(ht.nhflux_u*up(ht.varIntSpa)+ht.nhflux_d*down(ht.varIntSpa))	W	Total net energy rate	Global	
ht.QInt	ht.intDom(ht.Qtot*ht.varIntSpa)+ht.intIntLine(ht.Qltot*ht.varIntSpa)+ht.intLine(ht.Qlrtot*ht.varIntSpa)+ht.intIntPnt(ht.Qprtot)+ht.intPnt(ht.Qprtot)-ht.intIntBnd(ht.ndflux_u*up(ht.varIntSpa)+ht.ndflux_d*down(ht.varIntSpa))	W	Total heat source	Global	
ht.id	1	1	Physics indicator	Domains 1–4	
ht.Wstr	0	W/m³	Total stress power	Domains 1–4	+ operation
ht.WstrInt	0	W	Total stress power	Global	+ operation
ht.Wtot	0	W/m³	Total work source	Domains 1–4	+ operation
ht.WBndTot_u	0	W/m²	Total work source, upside	Boundaries 6, 9, 12	+ operation
ht.WBndTot_d	0	W/m²	Total work source, downside	Boundaries 1–22	+ operation
ht.WInt	0	W	Total work source	Global	+ operation
ht.varIntSpa	ht.d	1	Intermediate variable	Domains 1–4	Meta

Fig 5.2.9 Table for Selection of the position in Cylinder 5

2.4.3. Solid 1

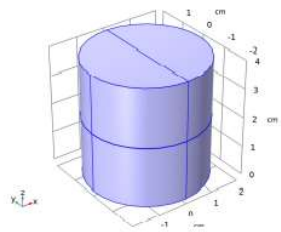

Solid 1

Selection

Geometric entity level	Domain
Selection	Geometry geom1: Dimension 3: All domains

Equations

$$\rho C_p \mathbf{u} \cdot \nabla T + \nabla \cdot \mathbf{q} = Q + Q_{ted}$$

$$\mathbf{q} = -k\nabla T$$

Fig 5.3.0 Selection of the position in Cylinder Solid 1

Heat Conduction, Solid

Thermodynamics, Solid

Settings

Description	Value
Density	From material
Heat capacity at constant pressure	From material

Fig 5.3.1 Table Selection of the settings in Cylinder solid

Coordinate System Selection

Settings

Description	Value
Coordinate system	Global coordinate system

Properties from material

Property	Material	Property group
Thermal conductivity	Steel AISI 4340	Basic
Density	Steel AISI 4340	Basic
Heat capacity at constant pressure	Steel AISI 4340	Basic
Thermal conductivity	Ceramic 1	YSZ
Density	Ceramic 1	YSZ
Heat capacity at constant pressure	Ceramic 1	YSZ
Thermal conductivity	7-8YSZ	Basic
Density	7-8YSZ	Basic
Heat capacity at constant pressure	7-8YSZ	Basic

Variables

Name	Expression	Unit	Description	Selection	Details
domflux.Tx	ht.dfluxx*ht.d	W/m²	Domain flux, x component	Domains 1–4	
domflux.Ty	ht.dfluxy*ht.d	W/m²	Domain flux, y component	Domains 1–4	
domflux.Tz	ht.dfluxz*ht.d	W/m²	Domain flux, z component	Domains 1–4	
ht.alphap	-d(ht.rho,Ty)/max(ht.rho,eps)	1/K	Isobaric compressibility coefficient	Domains 1–4	
ht.DeltaH	integrate(subst(ht.Cp,ht.solid1.minput_pressure,ht.pref),T,ht.DeltaH_Tlow,T)+integrate(ht.mu(T,ht.solid1.minput_pressure,ht.DeltaH_plow,ht.pA)	J/kg	Sensible enthalpy	Domains 1–4	+ operation
ht.H	ht.HRef+ht.DeltaH	J/kg	Enthalpy	Domains 1–4	+ operation
ht.Ei	ht.H	J/kg	Internal energy	Domains 1–4	+ operation
ht.Ek	0.5*(ht.ux^2+ht.uy^2+ht.uz^2)	J/kg	Kinetic energy	Domains 1–4	+ operation
ht.dfluxx	-ht.k_effxx*Tx-ht.k_effxy*Ty-ht.k_effxz*Tz	W/m²	Conductive heat flux, x component	Domains 1–4	+ operation
ht.dfluxy	-ht.k_effyx*Tx-ht.k_effyy*Ty-ht.k_effyz*Tz	W/m²	Conductive heat flux, y component	Domains 1–4	+ operation
ht.dfluxz	-ht.k_effzx*Tx-ht.k_effzy*Ty-ht.k_effzz*Tz	W/m²	Conductive heat flux, z component	Domains 1–4	+ operation
ht.dfluxtestx	-ht.k_effxx*test(Tx)-ht.k_effxy*test(Ty)-ht.k_effxz*test(Tz)	W/m²	Conductive heat flux, x component	Domains 1–4	+ operation
ht.dfluxtesty	-ht.k_effyx*test(Tx)-ht.k_effyy*test(Ty)-ht.k_effyz*test(Tz)	W/m²	Conductive heat flux, y component	Domains 1–4	+ operation
ht.dfluxtestz	-ht.k_effzx*test(Tx)-ht.k_effzy*test(Ty)-ht.k_effzz*test(Tz)	W/m²	Conductive heat flux, z component	Domains 1–4	+ operation
ht.cfluxx	ht.rho*ht.ux*ht.Ei	W/m²	Convective heat flux, x component	Domains 1–4	+ operation
ht.cfluxy	ht.rho*ht.uy*ht.Ei	W/m²	Convective heat flux, y component	Domains 1–4	+ operation
ht.cfluxz	ht.rho*ht.uz*ht.Ei	W/m²	Convective heat flux, z component	Domains 1–4	+ operation
ht.tefluxx	ht.dfluxx+ht.thfluxx	W/m²	Total energy flux, x component	Domains 1–4	+ operation
ht.tefluxy	ht.dfluxy+ht.thfluxy	W/m²	Total energy flux, y component	Domains 1–4	+ operation
ht.tefluxz	ht.dfluxz+ht.thfluxz	W/m²	Total energy flux, z component	Domains 1–4	+ operation
ht.thfluxx	ht.rho*ht.ux*ht.H0	W/m²	Total enthalpy flux, x component	Domains 1...4	+ operation

Fig 5.3.2 Table Selection of the Coordinate System selection 1

ht.tdfluxy	ht.rho*ht.uy*ht.H0	W/m²	Total enthalpy flux, y component	Domains 1–4	+ operation
ht.tdfluxz	ht.rho*ht.uz*ht.H0	W/m²	Total enthalpy flux, z component	Domains 1–4	+ operation
ht.ndflux_u	-ndflux_spotial(T)*up(ht.varIntSpa)	W/m²	Internal normal conductive heat flux, upside	Boundaries 6, 9, 12	+ operation
ht.ndflux_d	-ndflux_spotial(T)*down(ht.varIntSpa)	W/m²	Internal normal conductive heat flux, downside	Boundaries 6, 9, 12	+ operation
ht.ndflux_d	-ndflux_spotial(T)*down(ht.varIntSpa)	W/m²	Internal normal conductive heat flux, downside	Boundaries 1–5, 7–8, 10–11, 13–22	+ operation
ht.dEdInt	ht.solid1.dEdInt	W	Total accumulated heat rate	Global	+ operation
ht.dEdOint	ht.solid1.dEdOint	W	Total accumulated energy rate	Global	+ operation
ht.Wstr	ht.pA*(d(ht.ux,x)+d(ht.uy,y)+d(ht.uz,z))	W/m³	Total stress power	Domains 1–4	+ operation
ht.Wstrint	ht.solid1.Wstrint	W	Total stress power	Global	+ operation
ht.Wint	ht.solid1.Wint	W	Total work source	Global	+ operation
ht.kxx	material.k11	W/(m·K)	Thermal conductivity, xx component	Domains 1–4	Meta
ht.kyx	material.k21	W/(m·K)	Thermal conductivity, yx component	Domains 1–4	Meta
ht.kzx	material.k31	W/(m·K)	Thermal conductivity, zx component	Domains 1–4	Meta
ht.kxy	material.k12	W/(m·K)	Thermal conductivity, xy component	Domains 1–4	Meta
ht.kyy	material.k22	W/(m·K)	Thermal conductivity, yy component	Domains 1–4	Meta
ht.kzy	material.k32	W/(m·K)	Thermal conductivity, zy component	Domains 1–4	Meta
ht.kxz	material.k13	W/(m·K)	Thermal conductivity, xz component	Domains 1–4	Meta
ht.kyz	material.k23	W/(m·K)	Thermal conductivity, yz component	Domains 1–4	Meta
ht.kzz	material.k33	W/(m·K)	Thermal conductivity, zz component	Domains 1–4	Meta
ht.k_iso	material.k_iso	W/(m·K)	Thermal conductivity, isotropic value	Domains 1–4	Meta
ht.rho	material.rho	kg/m³	Density	Domains 1–4	Meta
ht.Cp	material.Cp	J/(kg·K)	Heat capacity at constant pressure	Domains 1–4	Meta
ht.solid1.pref	1[atm]	Pa	Reference pressure level	Domains 1–4	
ht.res_T	-ht.k_effxx*Tx-ht.k_effxy*Ty-ht.k_effxz*Tz-ht.k_effyx*Tx-ht.k_effyy*Ty-ht.k_effyz*Tz-ht.k_effzx*Tx-ht.k_effzy*Ty-ht.k_effzz*Tz-ht.qs+ht.qs_cog)+T-ht.C_eff*(ht.ux*Tx+ht.uy*Ty+ht.uz*Tz)-ht.D_Hx*Tx-ht.D_Hy*Ty-ht.D_Hz*Tz-ht.rhoCpUlx*Tx-ht.rhoCpUly*Ty-ht.rhoCpUlz*Tz-ht.Q-ht.Qcog	W/m³	Equation residual	Domains 1–4	+ operation
ht.pA	ht.pref	Pa	Absolute pressure	Domains 1–4	
ht.Qmet	0	W/m³	Metabolic heat source	Domains 1–4	+ operation
ht.pref	ht.solid1.pref	Pa	Reference pressure level	Domains 1–4	
ht.Delta0_Tlow	ht.Tref	K	Temperature lower bound for enthalpy evaluation	Domains 1–4	
ht.Delta0_plow	ht.pref	Pa	Pressure lower bound for enthalpy evaluation	Domains 1–4	
ht.muJT	0	m³/kg	Thomson-Joule-coefficient	Domains 1–4	
ht.alphap_ref	-d(root.comp1.ht.rhoref,ht.Tref)/max(root.comp1.ht.rhoref,eps)	1/K		Domains 1–4	

Fig 5.3.3 Selection of the table position in Variable iteration

			Reference isobaric compressibility coefficient		
ht.alphapT	ht.alphap*T	1	Help variable	Domains 1-4	
ht.rhoInit	subst(ht.rho,T,ht.Tinit,minput.pA,ht.pref)	kg/m³	Initial density	Domains 1-4	
ht.rho_eff	ht.rho	kg/m³	Effective density	Domains 1-4	
ht.C_eff	ht.rho*ht.Cp	J/(m³·K)	Effective volumetric heat capacity	Domains 1-4	
ht.k_effxx	ht.kxx	W/(m·K)	Effective thermal conductivity, xx component	Domains 1-4	
ht.k_effyx	ht.kyx	W/(m·K)	Effective thermal conductivity, yx component	Domains 1-4	
ht.k_effzx	ht.kzx	W/(m·K)	Effective thermal conductivity, zx component	Domains 1-4	
ht.k_effxy	ht.kxy	W/(m·K)	Effective thermal conductivity, xy component	Domains 1-4	
ht.k_effyy	ht.kyy	W/(m·K)	Effective thermal conductivity, yy component	Domains 1-4	
ht.k_effzy	ht.kzy	W/(m·K)	Effective thermal conductivity, zy component	Domains 1-4	
ht.k_effxz	ht.kxz	W/(m·K)	Effective thermal conductivity, xz component	Domains 1-4	
ht.k_effyz	ht.kyz	W/(m·K)	Effective thermal conductivity, yz component	Domains 1-4	
ht.k_effzz	ht.kzz	W/(m·K)	Effective thermal conductivity, zz component	Domains 1-4	
ht.kappaTxx	0	W/(m·K)	Turbulent thermal conductivity, xx component	Domains 1-4	
ht.kappaTyx	0	W/(m·K)	Turbulent thermal conductivity, yx component	Domains 1-4	
ht.kappaTzx	0	W/(m·K)	Turbulent thermal conductivity, zx component	Domains 1-4	
ht.kappaTxy	0	W/(m·K)	Turbulent thermal conductivity, xy component	Domains 1-4	
ht.kappaTyy	0	W/(m·K)	Turbulent thermal conductivity, yy component	Domains 1-4	
ht.kappaTzy	0	W/(m·K)	Turbulent thermal conductivity, zy component	Domains 1-4	
ht.kappaTxz	0	W/(m·K)	Turbulent thermal conductivity, xz component	Domains 1-4	
ht.kappaTyz	0	W/(m·K)	Turbulent thermal conductivity, yz component	Domains 1-4	
ht.kappaTzz	0	W/(m·K)	Turbulent thermal conductivity, zz component	Domains 1-4	
ht.kmean	(ht.k_effxx+ht.k_effyy+ht.k_effzzy)/3	W/(m·K)	Mean effective thermal conductivity	Domains 1-4	
ht.ux	0	m/s	Velocity field, x component	Domains 1-4	+ operation
ht.uy	0	m/s	Velocity field, y component	Domains 1-4	+ operation
ht.uz	0	m/s	Velocity field, z component	Domains 1-4	+ operation
ht.cellPe	0.5*ht.rho*ht.Cp*h*sqrt(ht.ux^2+ht.uy^2+ht.uz^2)/ht.kmean	1	Cell Peclet number	Domains 1-4	
ht.gradTx	Tx	K/m		Domains 1-4	

Fig 5.3.4 Table of variable in iterative values

			Temperature gradient, x component		
ht.gradTy	Ty	K/m	Temperature gradient, y component	Domains 1–4	
ht.gradTz	Tz	K/m	Temperature gradient, z component	Domains 1–4	
ht.gradTmag	sqrt(ht.gradTx^2+ht.gradTy^2+ht.gradTz^2)	K/m	Temperature gradient magnitude	Domains 1–4	
ht.alphaTdxx	ht.k_effxx/ht.C_eff	m²/s	Thermal diffusivity, xx component	Domains 1–4	
ht.alphaTdyx	ht.k_effyx/ht.C_eff	m²/s	Thermal diffusivity, yx component	Domains 1–4	
ht.alphaTdzx	ht.k_effzx/ht.C_eff	m²/s	Thermal diffusivity, zx component	Domains 1–4	
ht.alphaTdxy	ht.k_effxy/ht.C_eff	m²/s	Thermal diffusivity, xy component	Domains 1–4	
ht.alphaTdyy	ht.k_effyy/ht.C_eff	m²/s	Thermal diffusivity, yy component	Domains 1–4	
ht.alphaTdzy	ht.k_effzy/ht.C_eff	m²/s	Thermal diffusivity, zy component	Domains 1–4	
ht.alphaTdxz	ht.k_effxz/ht.C_eff	m²/s	Thermal diffusivity, xz component	Domains 1–4	
ht.alphaTdyz	ht.k_effyz/ht.C_eff	m²/s	Thermal diffusivity, yz component	Domains 1–4	
ht.alphaTdzz	ht.k_effzz/ht.C_eff	m²/s	Thermal diffusivity, zz component	Domains 1–4	
ht.alphaTdMean	ht.kmean/ht.C_eff	m²/s	Mean thermal diffusivity	Domains 1–4	
ht.Tradu	ht.Tu	K	Upside temperature	Domains 1–4	
ht.Tradu	ht.Tu	K	Upside temperature	Boundaries: 1–22	
ht.Tradd	ht.Td	K	Downside temperature	Domains 1–4	
ht.Tradd	ht.Td	K	Downside temperature	Boundaries: 1–22	
ht.solid1.dEiInt	ht.solid1.intDom((ht.dEi-ht.Qm*ht.Ei)*ht.varIntSpa)	W	Total accumulated heat rate	Global	
ht.dEi	0	W/m³	Total accumulated heat rate density	Domains 1–4	
ht.solid1.dEi0Int	ht.solid1.intDom((ht.dEi0-ht.Qm*ht.H)*ht.varIntSpa)	W	Total accumulated energy rate	Global	
ht.dEi0	0	W/m³	Total accumulated energy rate density	Domains 1–4	
ht.solid1.ntfluxInt	ht.solid1.intExtBnd(ht.ntflux*ht.varIntSpa)+ht.solid1.intExtBndUp(ht.ntflux_u*up(ht.varIntSpa))+ht.solid1.intExtBndDown(ht.ntflux_d*down(ht.varIntSpa))+ht.solid1.intIntBnd(ht.ncflux_u*up(ht.varIntSpa)+ht.ncflux_d*down(ht.varIntSpa))	W	Total net heat rate	Global	
ht.solid1.nncfluxInt	ht.solid1.intExtBnd(ht.nncflux*ht.varIntSpa)+ht.solid1.intExtBndUp(ht.nncflux_u*up(ht.varIntSpa))+ht.solid1.intExtBndDown(ht.nncflux_d*down(ht.varIntSpa))+ht.solid1.intIntBnd(ht.nthflux_u*up(ht.varIntSpa)+ht.nthflux_d*down(ht.varIntSpa))	W	Total net energy rate	Global	
ht.solid1.Qint	ht.solid1.intDom(ht.Qtot*ht.varIntSpa)+ht.solid1.intInt1.inc(ht.Qtot*ht.varIntSpa)+ht.intLinc(subst(ht.Qtot,ht.id,isdefined(ht.solid1.id))*ht.varIntSpa)+ht.solid1.intIntPnt(ht.Qptot)+ht.intPnt(subst(ht.Qptot,ht.id,isdefined(ht.solid1.id)))+ht.solid1.intIntBnd(ht.ndflux_u*up(ht.varIntSpa)+ht.ndflux_d*down(ht.varIntSpa))	W	Total heat source	Global	
ht.solid1.WstrInt	ht.solid1.intDom(ht.Wstr*ht.varIntSpa)	W	Total stress power	Global	
ht.solid1.WInt	ht.solid1.intDom(ht.Wtot*ht.varIntSpa)+ht.solid1.intBndUp(ht.WBndTot_u*up(ht.varIntSpa))+ht.solid1.intBndDown(ht.WBndTot_d*down(ht.varIntSpa))	W	Total work source	Global	
ht.D_Hx	0	W/(m²·K)	Enthalpy diffusion coefficient, x component	Domains 1–4	
ht.D_Hy	0	W/(m²·K)	Enthalpy diffusion coefficient, y component	Domains 1–4	

Fig 5.3.5 Table of variable in iterative values

ht.D_Hz	0	W/(m²·K)	Enthalpy diffusion coefficient, z component	Domains 1–4	
ht.Q_H	ht.D_Hx*Tx+ht.D_Hy*Ty+ht.D_Hz*Tz	W/m²	Enthalpy diffusion flux	Domains 1–4	
ht.rhoICplUlx	0	W/(m²·K)	Heat transfer coefficient, liquid water transport, x component	Domains 1–4	
ht.rhoICplUly	0	W/(m²·K)	Heat transfer coefficient, liquid water transport, y component	Domains 1–4	
ht.rhoICplUlz	0	W/(m²·K)	Heat transfer coefficient, liquid water transport, z component	Domains 1–4	
ht.timeDerivative	0	K/s	Temperature, first time derivative	Domains 1–4	
ht.gamma	1	1	Ratio of specific heats	Domains 1–4	
ht.Trho	ht.Tref	K	Temperature for density evaluation	Domains 1–4	
ht.dflupaque	1	1	Default opacity	Domains 1–4	
ht.helem	h_spatial	m	Element size	Domains 1–4	

Fig 5.3.6 Table of variable in iterative values

Shape functions

Name	Shape function	Unit	Description	Shape frame	Selection
T	Lagrange (Quadratic)	K	Temperature	Spatial	Domains 1–4

Fig 5.3.7 Table of shape function units

Weak Expressions

Weak expression	Integration order	Integration frame	Selection
ht.streamline	4	Spatial	Domains 1–4
(ht.dfluxx*test(Tx)+ht.dfluxy*test(Ty)+ht.dfluxz*test(Tz))*ht.d	4	Spatial	Domains 1–4
ht.C_eff*(ht.ux*Tx+ht.uy*Ty+ht.uz*Tz)*test(T)*ht.d	4	Spatial	Domains 1–4

Fig 5.3.7.1 Table of work expressions

2.4.4. Initial Values 1

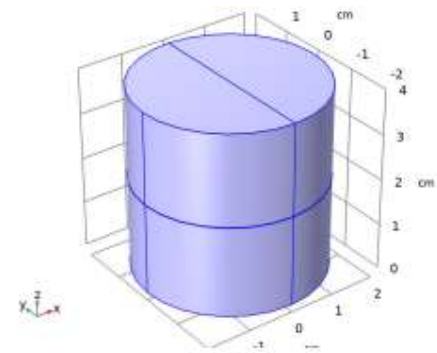

Initial Values 1

Selection

Geometric entity level	Domain
Selection	Geometry geom1: Dimension 3: All domains

Fig 5.3.7.2 Table of Initial values

Initial Values

Settings

Description	Value
Temperature	User defined
Temperature	293.15[K]

Fig 5.3.8 Table of settings in initial values

Variables

Name	Expression	Unit	Description	Selection
ht.Tinit	293.15[K]	K	Temperature	Domains 1–4

Fig 5.3.9 Table of variables in temperature

2.4.5. Thermal Insulation 1

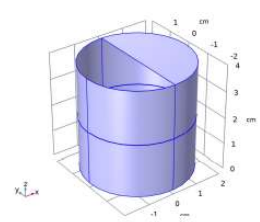

Thermal Insulation 1

Fig 5.4.0 Thermal insulation in cylinder 1

Selection

Geometric entity level	Boundary
Selection	Geometry geom1: Dimension 2: All boundaries

Equations

$-\mathbf{n}\cdot\mathbf{q}=0$

Fig 5.4.1 Table of selection boundary level

Variables

Name	Expression	Unit	Description	Selection
ht.ins1.ntfluxInt	ht.ins1.intExtBnd(ht.ntflux*ht.varIntSpa)+ht.ins1.intIntBnd(ht.ncflux_u*up(ht.varIntSpa)+ht.ncflux_d*down(ht.varIntSpa))	W	Total net heat rate	Global
ht.ins1.nteffluxInt	ht.ins1.intExtBnd(ht.nteflux*ht.varIntSpa)+ht.ins1.intIntBnd(ht.nthflux_u*up(ht.varIntSpa)+ht.nthflux_d*down(ht.varIntSpa))	W	Total net energy rate	Global
ht.ins1.ntfluxInt_u	ht.ins1.intIntBnd(ht.ntflux_u*up(ht.varIntSpa))	W	Total net heat rate, upside	Global
ht.ins1.nteffluxInt_u	ht.ins1.intIntBnd(ht.nteflux_u*up(ht.varIntSpa))	W	Total net energy rate, upside	Global
ht.ins1.ntfluxInt_d	ht.ins1.intIntBnd(ht.ntflux_d*down(ht.varIntSpa))	W	Total net heat rate, downside	Global
ht.ins1.nteffluxInt_d	ht.ins1.intIntBnd(ht.nteflux_d*down(ht.varIntSpa))	W	Total net energy rate, downside	Global
ht.ins1.Tave	nojac(ht.ins1.intBnd(ht.varIntSpa*ht.rho*ht.Cp*T*max(abs(ht.ux*ht.nxmesh+ht.uy*ht.nymesh+ht.uz*ht.nzmesh),eps))/nojac(ht.ins1.intBnd(ht.varIntSpa*ht.rho*ht.Cp*max(abs(ht.ux*ht.nxmesh+ht.uy*ht.nymesh+ht.uz*ht.nzmesh),eps)))	K	Weighted average temperature	Global

Fig 5.4.2 Table for selection of Variables

Shape functions

Name	Shape function	Unit	Description	Shape frame	Selection	Details
T	Lagrange (Quadratic)	K	Temperature	Spatial	No boundaries	Slit
T	Lagrange (Quadratic)	K	Temperature	Material	No boundaries	Slit
T	Lagrange (Quadratic)	K	Temperature	Geometry	No boundaries	Slit
T	Lagrange (Quadratic)	K	Temperature	Mesh	No boundaries	Slit

Fig 5.4.3 Table of Shape function in quadratic function

2.4.6. Temperature 1

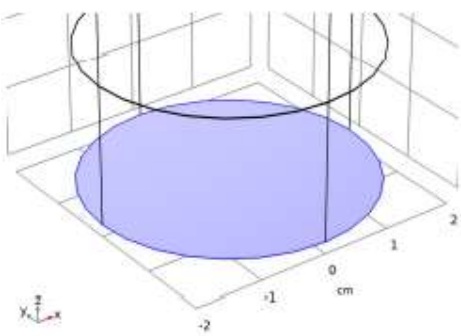

Temperature 1

Fig 5.4.4 figure of temperature 1

Selection

Geometric entity level	Boundary
Selection	Geometry geom1: Dimension 2: Boundary 3

Equations

$T = T_0$

Fig 5.4.5 Table of Selection of geometry equations

Temperature

Settings

Description	Value
Temperature	User defined
Temperature	293.15[K]

Fig 5.4.6 Table of Shape function in temperature

Variables

Name	Expression	Unit	Description	Selection	Details
ht.T0	293.15[K]	K	Temperature	Boundary 3	+ operation
ht.temp1.ntfluxInt	ht.temp1.intExtBnd(ht.ntflux*ht.varIntSpa)+ht.temp1.intIntBnd(ht.ncflux_u*up(ht.varIntSpa) +ht.ncflux_d*down(ht.varIntSpa))	W	Total net heat rate	Global	
ht.temp1.nteffluxInt	ht.temp1.intExtBnd(ht.nteflux*ht.varIntSpa)+ht.temp1.intIntBnd(ht.ntfflux_u*up(ht.varIntSpa) +ht.ntfflux_d*down(ht.varIntSpa))	W	Total net energy rate	Global	
ht.temp1.ntfluxInt_u	ht.temp1.intIntBnd(ht.ntflux_u*up(ht.varIntSpa))	W	Total net heat rate, upside	Global	
ht.temp1.nteffluxInt_u	ht.temp1.intIntBnd(ht.nteflux_u*up(ht.varIntSpa))	W	Total net energy rate, upside	Global	
ht.temp1.ntfluxInt_d	ht.temp1.intIntBnd(ht.ntflux_d*down(ht.varIntSpa))	W	Total net heat rate, downside	Global	
ht.temp1.nteffluxInt_d	ht.temp1.intIntBnd(ht.nteflux_d*down(ht.varIntSpa))	W	Total net energy rate, downside	Global	
ht.temp1.Tave	nojac(ht.temp1.intBnd(ht.varIntSpa*ht.rho*ht.Cp*T*max(abs (ht.ux*ht.nxmesh+ht.uy*ht.nymesh+ht.uz*ht.nzmesh),eps))/nojac(ht.temp1.intBnd (ht.varIntSpa*ht.rho*ht.Cp*max(abs(ht.ux*ht.nxmesh+ht.uy*ht.nymesh+ht.uz*ht.nzmesh),eps)))	K	Weighted average temperature	Global	

Fig 5.4.7 Table of variables in shape function

Constraints

Constraint	Constraint force	Shape function	Selection	Details
ht.T0-ht.Tvar	test(ht.T0-ht.Tvar)	Lagrange (Quadratic)	Boundary 3	Elemental

Fig 5.4.8 Table of Constraint in shape function

2.4.7. Temperature 2

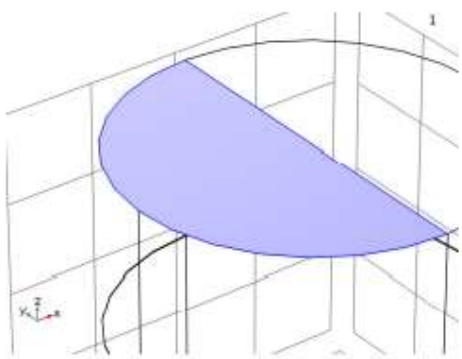

Temperature 2

Fig 5.4.9 Figure of temperature 2 selected profile

Selection

Geometric entity level	Boundary
Selection	Geometry geom1: Dimension 2: Boundary 13

Equations

$T = T_0$

Fig 5.5.0 Table of Selection in Boundary

Temperature

Settings

Description	Value
Temperature	User defined
Temperature	T_hot

Fig 5.5.1 Table of Temperature user defined

Variables

Name	Expression	Unit	Description	Selection	Details
ht.T0	T_hot	K	Temperature	Boundary 13	+ operation
ht.temp2.ntfluxInt	ht.temp2.intExtBnd(ht.ntflux*ht.varIntSpa)+ht.temp2.intIntBnd(ht.ncflux_u*up(ht.varIntSpa) +ht.ncflux_d*down(ht.varIntSpa))	W	Total net heat rate	Global	
ht.temp2.ntefluxInt	ht.temp2.intExtBnd(ht.nteflux*ht.varIntSpa)+ht.temp2.intIntBnd(ht.nthflux_u*up(ht.varIntSpa) +ht.nthflux_d*down(ht.varIntSpa))	W	Total net energy rate	Global	
ht.temp2.ntfluxInt_u	ht.temp2.intIntBnd(ht.ntflux_u*up(ht.varIntSpa))	W	Total net heat rate, upside	Global	
ht.temp2.ntefluxInt_u	ht.temp2.intIntBnd(ht.nteflux_u*up(ht.varIntSpa))	W	Total net energy rate, upside	Global	
ht.temp2.ntfluxInt_d	ht.temp2.intIntBnd(ht.ntflux_d*down(ht.varIntSpa))	W	Total net heat rate, downside	Global	
ht.temp2.ntefluxInt_d	ht.temp2.intIntBnd(ht.nteflux_d*down(ht.varIntSpa))	W	Total net energy rate, downside	Global	
ht.temp2.Tave	nojac(ht.temp2.intBnd(ht.varIntSpa*ht.rho*ht.Cp*T*max(abs (ht.ux*ht.nxmesh+ht.uy*ht.nymesh+ht.uz*ht.nzmesh),eps)))/nojac(ht.temp2.intBnd (ht.varIntSpa*ht.rho*ht.Cp*max(abs(ht.ux*ht.nxmesh+ht.uy*ht.nymesh+ht.uz*ht.nzmesh),eps)))	K	Weighted average temperature	Global	

Fig 5.5.2 Table of Variable expression selection

Constraints

Constraint	Constraint force	Shape function	Selection	Details
ht.T0-ht.Tvar	test(ht.T0-ht.Tvar)	Lagrange (Quadratic)	Boundary 13	Elemental

Fig 5.5.3 Table of constraint shape function

2.5. Mesh 1

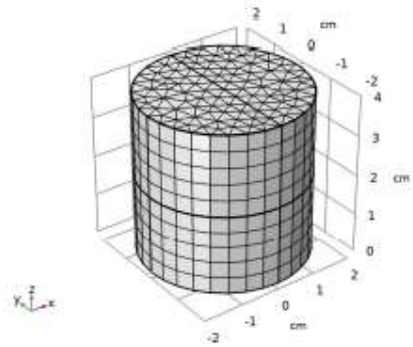

Mesh 1

Mesh statistics

Description	Value
Minimum element quality	0.01019
Average element quality	0.6489
Prism	2856
Triangle	1020
Quad	448
Edge element	226
Vertex element	20

Fig 5.5.4 Table of selection Mesh 1

2.5.1. Size (size)

Settings

Description	Value
Maximum element size	0.4
Minimum element size	0.072
Curvature factor	0.6
Resolution of narrow regions	0.5
Maximum element growth rate	1.5

Fig 5.5.5 Table of size settings

2.5.2. Free Triangular 1 (ftri1)

Selection

Geometric entity level	Boundary
Selection	Geometry geom1: Dimension 2: Boundaries 13, 18

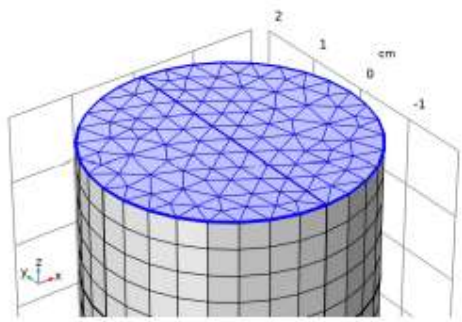

Free Triangular 1

Fig 5.5.6 Table of Selection free Triangular 1

2.5.3. Swept 1 (swe1)

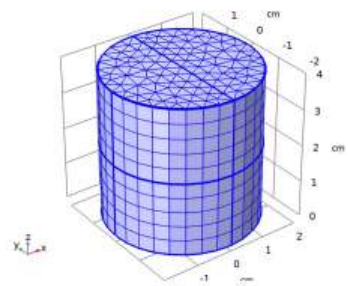

Swept 1

Fig 5.5.7 figure of Swept 1

Distribution 1 (dis1)

Selection

Geometric entity level	*Domain*
Selection	Geometry geom1: Dimension 3: Domains 2–3

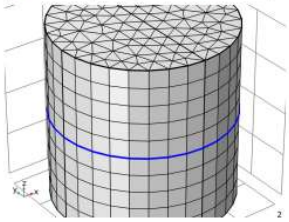

Distribution 1

Settings

Description	Value
Number of elements	2

Fig 5.5.8 table for distribution 1

4.1. Stationary

Study settings

Description	Value
Include geometric nonlinearity	Off

Physics and variables selection

Physics interface	Discretization
Heat Transfer in Solids (ht)	physics

Mesh selection

Geometry	Mesh
Geometry 1 (geom1)	mesh1
Geometry 2 (geom2)	mesh2

Fig 5.5.9 Table of Study settings

4.2. Solver Configurations

4.2.1. Solution 1

Compile Equations: Stationary (st1)

Study and step

Description	Value
Use study	Study 1
Use study step	Stationary

Log

```
<---- Compile Equations: Stationary in Study 1/Solution 1 (sol1) ----------
Started at Oct 14, 2020 10:24:12 AM.
Geometry shape function: Quadratic Lagrange
Running on 2 x Intel(R) Xeon(R) Gold 6128 CPU at 3.40 GHz.
Using 2 sockets with 12 cores in total on vale.
Available memory: 95.02 GB.
Time: 1 s.
Physical memory: 6.67 GB
Virtual memory: 16.11 GB
Ended at Oct 14, 2020 10:24:13 AM.
----- Compile Equations: Stationary in Study 1/Solution 1 (sol1) ---------->
```

Fig 5.6.0 compile equations of study 1

Dependent Variables 1 (v1)

General

Description	Value
Defined by study step	Stationary

Log

```
<---- Dependent Variables 1 in Study 1/Solution 1 (sol1) ----------
Started at Oct 14, 2020 10:24:13 AM.
Solution time: 0 s.
Physical memory: 6.67 GB
Virtual memory: 16.11 GB
Ended at Oct 14, 2020 10:24:13 AM.
----- Dependent Variables 1 in Study 1/Solution 1 (sol1) ---------->
```

Fig 5.6.1 dependent variables equations of study 1

Temperature (comp1.T) (comp1_T)

General

Description	Value
Field components	comp1.T
Internal variables	{comp1.uflux.T, comp1.dflux.T}

Fig 5.6.2 Temperature of study 1

Stationary Solver 1 (s1)

General

Description	Value
Defined by study step	Stationary

Log

```
<---- Stationary Solver 1 in Study 1/Solution 1 (sol1) ----------
Started at Oct 14, 2020 10:24:13 AM.
Linear solver
Number of degrees of freedom solved for: 12789 (plus 5725 internal DOFs).
Symmetric matrices found.
Scales for dependent variables:
Temperature (comp1.T): 2.9e+02
Orthonormal null-space function used.
Iter    SolEst    Damping    Stepsize #Res #Jac #Sol  LinErr  LinRes
  1      0.61   1.0000000      0.61    1    1    1  4.4e-15  4.6e-15
Solution time: 1 s.
Physical memory: 6.67 GB
Virtual memory: 16.11 GB
Ended at Oct 14, 2020 10:24:14 AM.
----- Stationary Solver 1 in Study 1/Solution 1 (sol1) ---------->
```

Fig 5.6.3 Stationary Solver of study 1

Fully Coupled 1 (fc1)

General

Description	Value
Linear solver	Direct, temperature (ht)

Method and termination

Description	Value
Initial damping factor	0.01
Minimum damping factor	1.0E-6
Maximum number of iterations	50
Termination criterion	Solution

Fig 5.6.4 compile equations of study 1

Direct, temperature (ht) (d1)

General

Description	Value
Solver	PARDISO
Pivoting perturbation	1.0E-13

Log

```
<---- Compile Equations: Stationary in Study 2/Solution 2 (sol2) ----------
Started at Oct 14, 2020 10:25:28 AM.
Geometry shape function: Quadratic Lagrange
Geometry shape function: Quadratic Lagrange
Geometry shape function: Quadratic Lagrange
Running on 2 x Intel(R) Xeon(R) Gold 6128 CPU at 3.40 GHz.
Using 2 sockets with 12 cores in total on vale.
Available memory: 95.02 GB.
Time: 3 s.
Physical memory: 6.67 GB
Virtual memory: 16.12 GB
Ended at Oct 14, 2020 10:25:31 AM.
----- Compile Equations: Stationary in Study 2/Solution 2 (sol2) ---------->
```

Fig 5.6.5 temperature of study 2

6. Study 3

Computation information

Computation time	7 s

Fig 5.6.6 computation of study 3

6.1. Stationary

Study settings

Description	Value
Include geometric nonlinearity	Off

Physics and variables selection

Physics interface	Discretization
Heat Transfer in Solids 2 (ht2)	physics

Mesh selection

Geometry	Mesh
Geometry 1 (geom1)	mesh1
Geometry 2 (geom2)	mesh2

Fig 5.6.7 Stationary of geometric study

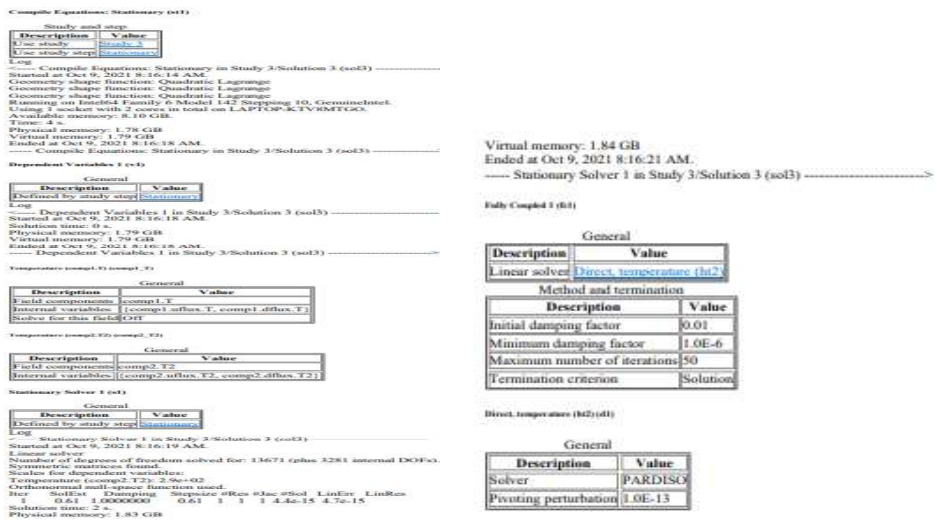

Fig 5.6.8 Compile equations Stationary

7. Results

7.1. 3D Approach

7.1.1. Plot Groups

Temperature (ht)

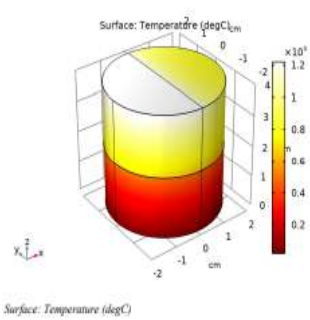

Fig 5.6.9 Results in surface temperature (degC)

Isothermal Contours (ht)

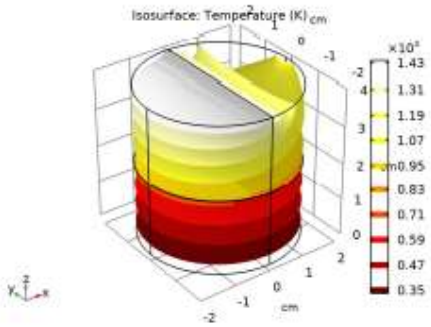

Fig 5.7.0 Results in surface temperature (degC)

7.2. 2D Approach

7.2.1. Plot Groups

Temperature (ht2)

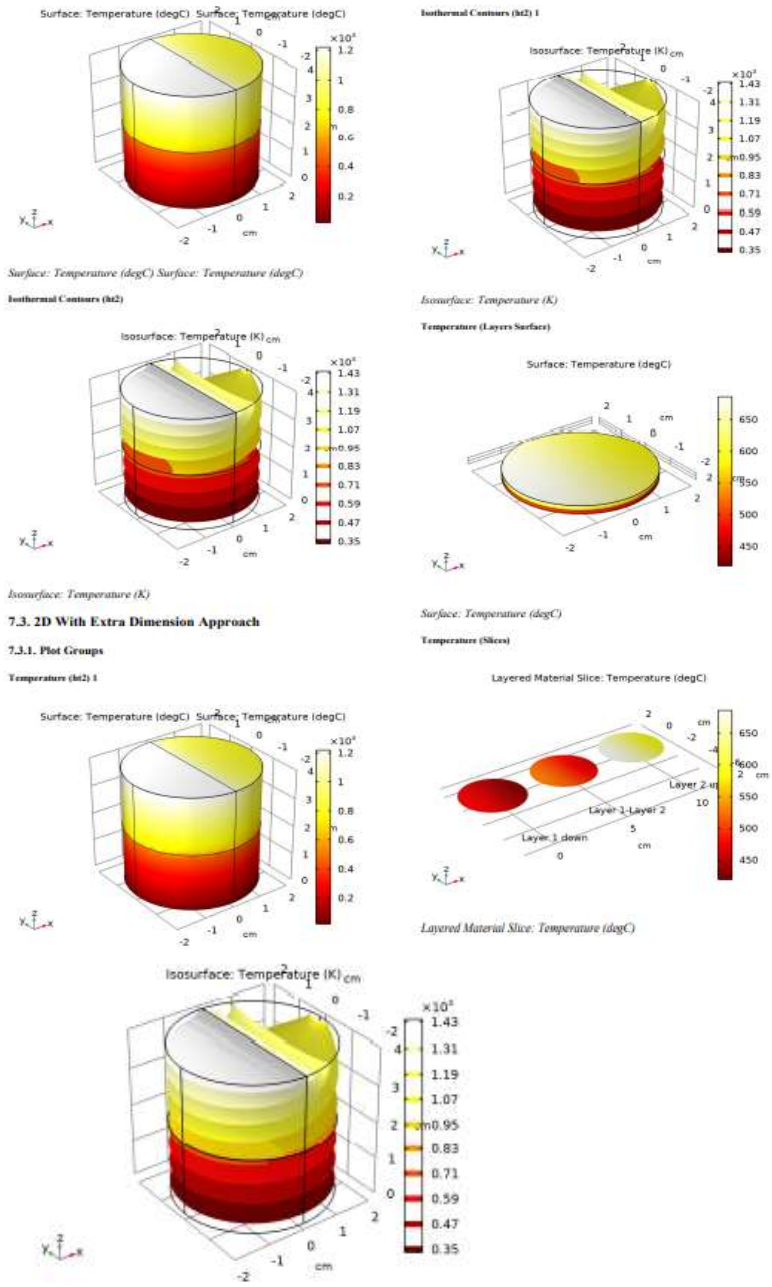

Fig 5.7.1 Results in 2D temperature (ht) approach (degC)

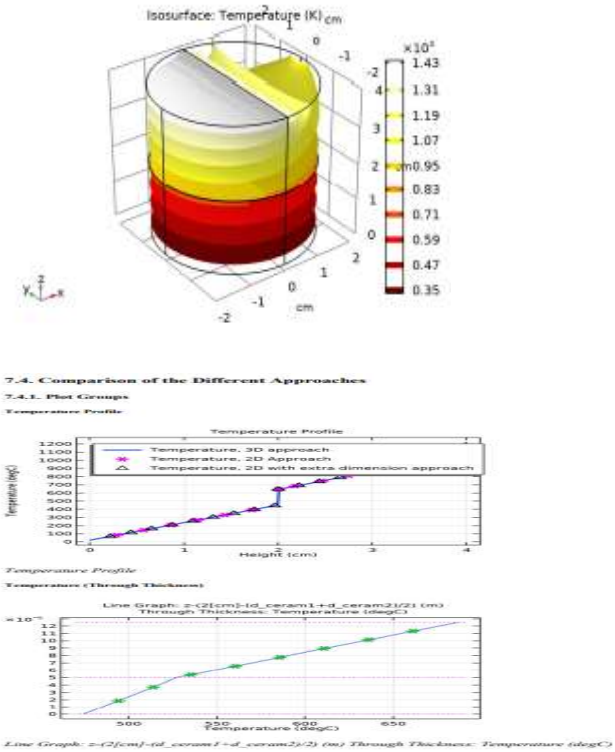

Fig 5.7.2 Results of different approach in temperature graph iso surface temperature (degC)

7.5. Datasets

7.5.1. Study 1/Solution 1

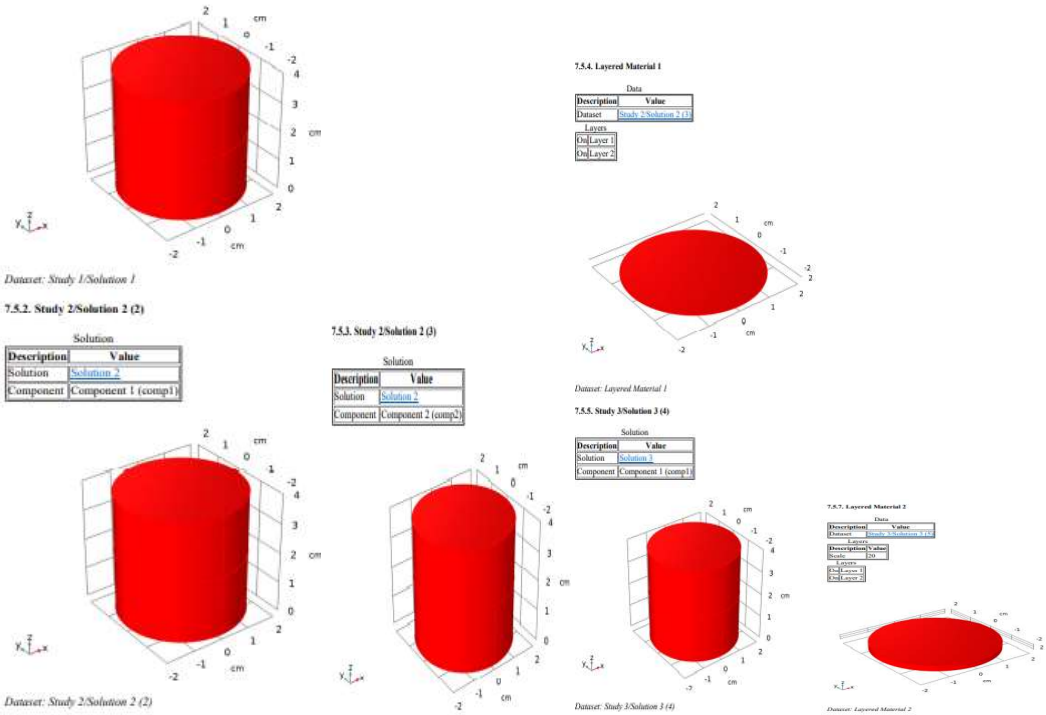

Fig 5.7.3 Results in study 2 of datasets

7.6. Derived Values

7.6.1. Global Evaluation 1

Output

Evaluated in Table 1

Data

Description	Value
Dataset	Study 1/Solution 1

Expressions

Expression	Unit	Description
T_ave_barrier	degC	Average of temperature in thermal barrier
T_ave_layer1	degC	Average of temperature in layer 1
T_ave_layer2	degC	Average of temperature in layer 2

Fig 5.7.4 Results in Global Evaluation 1

7.6.2. Global Evaluation 2

Data

Description	Value
Dataset	Study 3/Solution 3 (5)

Expressions

Expression	Unit	Description
T_ave_barrier	degC	Average of temperature in thermal barrier
T_ave_layer1	degC	Average of temperature in layer 1
T_ave_layer2	degC	Average of temperature in layer 2

Fig 5.7.5 Results in Global Evaluation 2

7.7. Tables

7.7.1. Table 1

Global Evaluation 1

Average of temperature in thermal barrier (degC)	Average of temperature in layer 1 (degC)	Average of temperature in layer 2 (degC)
530.05	472.64	568.33

Fig 5.7.6 Results in table 1 Global Evaluation 1

7.7.2. Table 2

Global Evaluation 2

Average of temperature in thermal barrier (degC)	Average of temperature in layer 1 (degC)	Average of temperature in layer 2 (degC)
530.26	472.98	568.45

Fig 5.7.7 Results in table 2 Global Evaluation 2

Performance of Pure ZrO2 :

Thermal Conductivity in W/(m-k)	**1.5**
Density in Kg/m3	4230
Hot temperature in Deg, C	1445.775
temperature thermal barrier in(Deg C)	530.5

Table 5.7.9 Table for Performance of Pure ZrO_2

Performance of 7-8 YSZ :

Thermal Conductivity in W/(m-k)	**1.5**
Density in Kg/m3	4230
Hot temperature in DegC	1445.775
temperature thermal barrier in(Deg C)	530.5

Table 5.8.0 Table for Performance of Pure ZrO_2

RESULTS AND DISCUSSIONS:

Sl no.	Type of mixer	Thermal Conductivity in W/(m-k)	Simulation
1.	Amorphous Al_2O_3 doped with YSZ	12	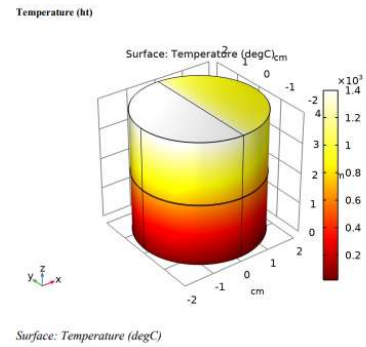
2.	Amorphous MoO_3 doped with YSZ	24.1	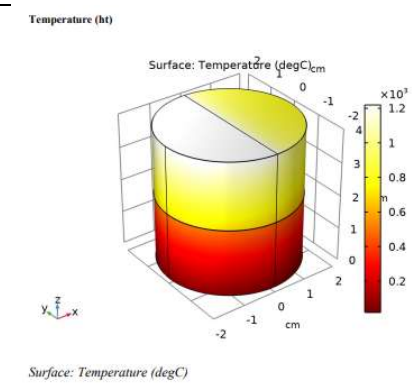
3.	Amorphous TiO_2 doped with YSZ	4.8	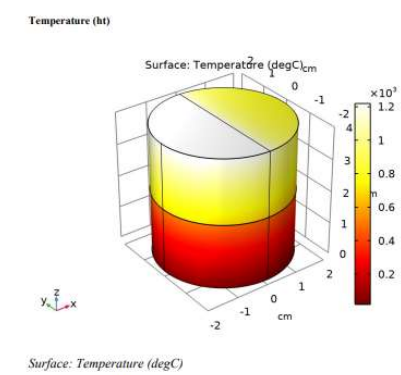
4.	PureZrO_2	1.5	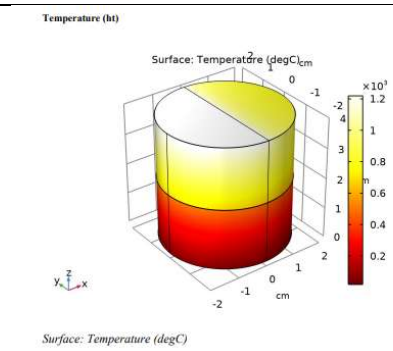

5.	ZrO_2	2.9	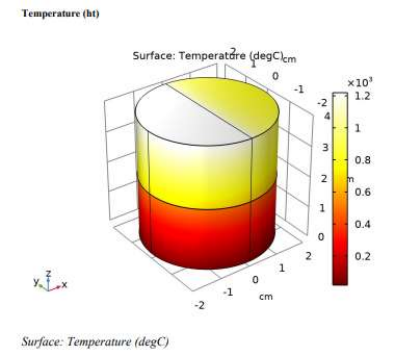
6.	7-8YSZ	0.5	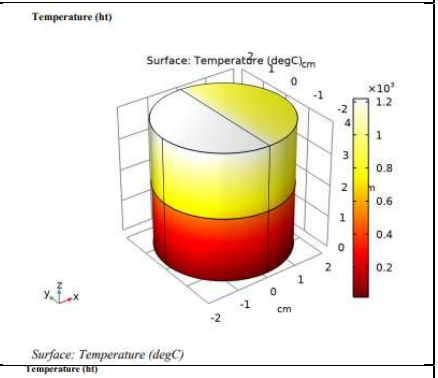
7.	80%ZrO_2+10%Y_2O_3+10%MoO_3	2.5632	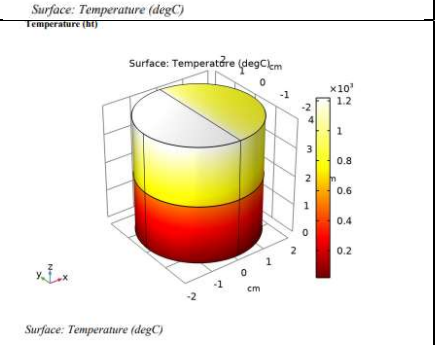
8.	90%ZrO_2+5%Y_2O_3+5%MoO_3	2.13	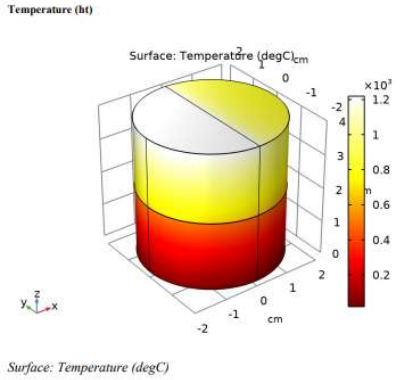

9.	80%ZrO_2+10%Y_2O_3+10%Al_2O_3	1.8	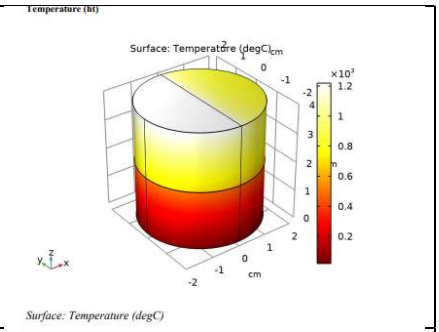
10.	90%ZrO_2+5%Y_2O_3+5%Al_2O_3	8.12	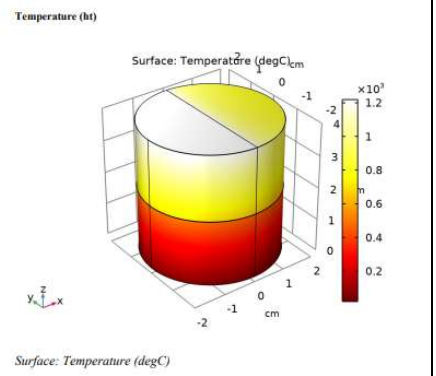
11.	80%ZrO_2+10%Y_2O_3+10%TiO_2	3.45	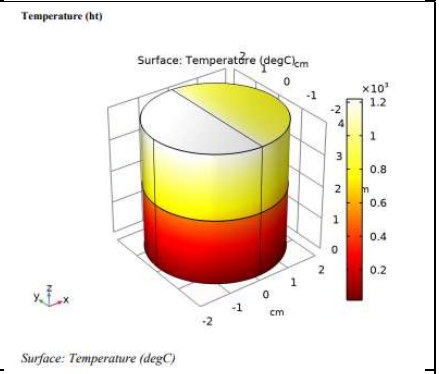
12.	90%ZrO_2+5%Y_2O_3+5%TiO_2	8.12	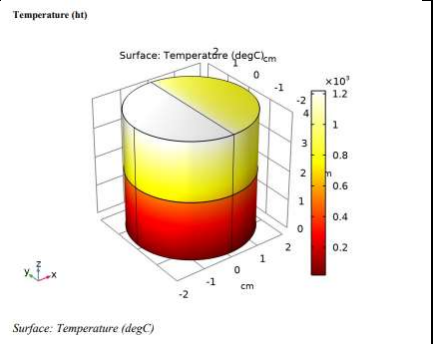

Table 5.7.8 Results of thermal barrier temperature profile

CONCLUSION

We have seen more heat dissipation and more barrier temperature in Pure ZrO_2 and 7-8 YSZ .By meshing and swept of finite element analysis according to the analysis two composites are have better performance comparatively.The pure ZrO_2 ,7-8 YSZ variants proved better by barrier temperatures.

We have seen more heat dissipation and more barrier temperature in Pure ZrO_2 and 7-8 YSZ .

By meshing and swept of finite element analysis according to the analysis two composites are have better performance comparatively.The pure ZrO_2 ,7-8 YSZ variants proved better by barrier temperatures. In the Computational approach the finite element analysis were done by the discretion of the elements and meshing were done by using the COMSOL Multiphyiscs software, In this the iteration values were taken by the literature review we found better results in the evaluation tables.

Amorphous Al_2O_3 doped yttria stabilized zirconia (YSZ) nano glass and glass ceramic materials prepared by simple mechanical ball milling method for TBC. Structural calculations performed by XRD technique. Al_2O_3 doped yttria stabilized zirconia (YSZ) nano glass ceramic TBC materials have major crystalline phase monoclinic ZrO_2 (ICSD # 15983). The computational method is adopted to predict mechanical and thermal properties of Al_2O_3 doped yttria stabilized zirconia (YSZ) nano glass ceramic TBC materials. 5 wt% Al_2O_3 doped yttria stabilized zirconia (YSZ) nano glass ceramic TBC material shows very good mechanical and thermal properties for thermal barrier coatings. 5 wt% Al_2O_3 doped yttria stabilized zirconia (YSZ) nano glass ceramic TBC materials have the highest bulk modulus, highest specific heat capacity, thermal diffusivity and thermal conductivity which which are increasing with increased temperature.

SCOPE OF FUTURE IMPROVEMENT

At last we have conclude that barrier temperature in Pure ZrO_2 and 7-8 YSZ.
Others TBC's similar performance but miniature difference in temperatures.
The nano glass and glass ceramic materials prepared by high energy ball milling and synthesized by taking the formula of [100-(x+y)] ZrO_2 + x Y_2O_3 + y (30 hours ball milled nano amorphous Al_2O_3 /TiO_2 /MoO_3) [here x=y= 5 and 10 wt%].
30 hours ball milled nano amorphous Al_2O_3 /TiO_2 /MoO_3 stabilized the yttria-zirconia (YSZ) crystalline structure and enhances their Thermal barrier coating performance effectively. Nanostructure glass and glass ceramics TBCs materials are characterized by X-ray powder diffraction (XRD).
The extent of the adding 30 hours ball milled nano amorphous Al_2O_3 /TiO_2 /MoO_3 to base nano glass expected to show the excellent specific heat capacity, thermal diffusivity, and thermal conductivity. The thermal diffusivity and thermal conductivity of the TBC coated substrate were lower than those of bare substrate and nano glass/glass ceramic coated substrate.
First principle/DFT calculations are a useful tool for predicting the mechanical and thermal properties of TBC materials. Here we are calculated thermal and mechanical properties. These two TBC's can further may undergo experimentally in future.

REFERENCES

- [1] Giannozzi, Paolo, Stefano Baroni, Nicola Bonini, Matteo Calandra, Roberto Car, Carlo Cavazzoni, Davide Ceresoli et al. "QUANTUM ESPRESSO: a modular and open-source software project for quantum simulations of materials." Journal of physics: Condensed matter 21, no. 39,p.p.395502, 2009.
- [2] Vanderbilt, David. "Soft self-consistent pseudopotentials in a generalized eigenvalue formalism." Physical Review B 41, no. 11,p.p. 7892, 1990.
- [3] Perdew, John P., Kieron Burke, and Matthias Ernzerhof. "Generalized gradient approximation made simple." Physical review letters 77, no. 18, p.p. 3865,1996.
- [4] Da Silva, Juarez LF, M. Veronica Ganduglia-Pirovano, Joachim Sauer, Veronika Bayer, and Georg Kresse. "Hybrid functionals applied to rare-earth oxides: The example of ceria." Physical Review B 75, no. 4, p.p. 045121, 2007.
- [5] G. Kresse, "Ab-Initio Molecular-Dynamics for Liquid-Metals," Journal of NonCrystalline Solids, vol. 193, pp. 222-229, Dec 1995.
- [6] P. F. Manicone, P. Rossi Iommetti, and L. Raffaelli, "An overview of zirconia ceramics: basic properties and clinical applications," Journal of Dentistry, vol. 35, pp. 819-26, 2007.
- [7] D. Vanderbilt, "Soft self-consistent pseudopotentials in a generalized eigenvalue formalism," Physical review. B, Condensed matter, vol. 41, pp. 7892-7895, 1990.
- [8] A. Togo, F. Oba, and I. Tanaka, "First-principles calculations of the ferroelastic transition between rutiletype and CaCl2-type SiO2 at high pressures," Physial Review B, vol. 78, p. 134106, 2008. 40
- [9] Naray-Szabo, S., Zeitschrift fuer Kristallographie, Kristallgeometrie, Kristallphysik, Kristallchemie (-144,1977), 94, 414, (1936).
- [10] Faucher, M., Golden Book of Phase Transitions, Wroclaw, 1, 1, (2002).

- [11] Dachille, F. Simons, P.Y., Acta Crystallographica (1,1948-23,1967), 23, 334, (1967)
- [12] Rietveld HM (1967) Line profiles of neutron powder-diffraction peaks for structure refinement. Acta Crystallogr 22(1):151-152.
- [13] Williamson GK, Hall WH (1953) X-ray line broadening from filed aluminium and wolfram. Acta Metall Mater 1(1): 22-31.
- [14] Momma K, Izumi F (2011) VESTA 3 for three-dimensional visualization of crystal, volumetric and morphology data. J Appl Crystallogr 44(6):1272-1276.